On the Speed of Sound in Neutron Stars

Sinan Altiparmak

Bachelor thesis

Johann Wolfgang Goethe Universität
Frankfurt am Main
Institut für theoretische Physik

Supervisor and first examiner: Prof. Dr. Luciano Rezzolla
Advisor and second examiner: Dr. Christian Ecker

Contents

Acknowledgements

I am deeply thankful to my supervisors Prof. Dr. Rezzolla and Dr. Christian Ecker for the possibility to work on this highly interesting project. By having taken me to the frontier of what is known, you have pushed and extended my skills to a level I did not thought possible and for which I am extremely thankful, especially given how hard I struggled with physics and mathematics in middle school. It was a true honor working with you. I also want to thank Alejandro Cruz-Osorio, Raphaël Duque, Konrad Topolski, Samuel Tootle, Lukas Weih and Cédric Jockel for continuous support and valuable advice along the way.

Moreover, I am greatly thankful to my friends and companions who supported and were there for me in challenging times by offering an open ear, hilarious bonfire-talks or their plain understanding. Thank you Robin, Till, Jonas, Rüya, Felix S., Amin, Flo, Matthias, Nils, Felix M, Peter A., Larissa. Without you, this would not have been possible and I am glad to have you in my life.

Special gratitude goes out to Rüya, Peter K. and Jonas with whom I spent a significant part of my bachelor-journey. It was such a fun time struggling through the problems with you and I will always fondly remember the endless hours we've spent flexin' those exercises.

Der allergrößte Dank gilt jedoch meiner Familie, allen voran Mama, Papa und Aylin sowie die Fraktionen Bornheim, Sprendlingen und Hennef. Für eure Unterstützung gibt es keine Worte - sie war essentiell dafür verantwortlich dass ich durchgezogen habe. Ihr seid mein größtes Glück.

Last but not least, I want to thank myself for persevering, pushing through, not losing focus and the unmeasureable amount of personal growth I will always associate with this time.

1 Introduction and Astrophysical Background

1.1 Neutron Stars as a Tool to Study Dense Matter

Neutron Stars are the densest objects in the universe that are not black holes. Binary Neutron Star mergers are significant sources of gravitational waves [1] and do hence serve as unique laboratories to study strongly interacting matter at high densities.

The existence of Neutron Stars was first proposed in 1933 by Walter Baade and Fritz Zwicky, which was only two years after the discovery of the neutron by James Chadwick. Because the light emitted by Neutron Stars was held to be too faint compared to that of usual stars, their study did not yield much progress in the decades after their proposal. This changed in 1967, when Franco Pacini proposed that spinning Neutron Stars would obtain strong magnetic fields, which would lead to the emission of electromagnetic waves. It took only two years until the discovery of this exact phenomenon, when Jocelyn Bell Burnell and Anthony Hewish detected periodic radio pulses from PSR B1919+21, giving also rise to the term "Pulsar" for rotating Neutron Stars which periodically emit light pulses. The next breakthrough discovery was not long in coming, when in 1974 Joseph Taylor and Russell Hulse discovered PSR B1913+16, the first binary pulsar system of two Neutron Stars orbiting around their common center of mass. The significance of this discovery is much bigger however: Albert Einstein predicted in his Theory of General Relativity, that accelerated bodies in close orbits lose kinetic energy due to the emission of gravitational waves, thus leading to a continuous decay of their orbit and ultimately to their collision. The orbital decay detected from PSR B1913+16 precisely matched the prediction of general relativity and thus served as the first indirect measurement of gravitational waves. The first direct measurement of gravitational waves produced by two colliding Neutron Stars was just done in August 2017 by the LIGO/Virgo collaboration, opening the possibility to learn about the dense matter present in Neutron Stars through the gravitational wave signals.

When a star with a mass greater than $8M_\odot$ leaves the main sequence and starts to produce iron, the nuclear fuel in the core will eventually deplete. Since iron has the highest binding energy-per nucleon, no net-energy would be generated when fusing it leading to a growing iron core inside the dying star which is under huge gravitational pressure. At this point, a core-collapse is only prevented by the degeneracy pressure of its constituent electrons. However, since nuclear fusion still undergoes in the outer layers of the star, further mass accretion onto the core causes it to ultimately exceed the Chandrasekhar limit of $1.4M_\odot$ [2] and thus triggers a type II supernova [3]. Because the collapsing core reaches densities several times that of nuclear saturation density, protons are turned into neutrons through electron capture which become degenerate. During this process, neutrinos are also generated. Because neutrinos sparsely interact with normal matter, they are able to escape the core and immensely cool it by carrying away massive amounts of energy. By doing this, these "thermal neutrinos" enable the formation of a stable Neutron Star. The newly born Neutron Star is now kept safe from gravitational collapse by a patchwork of mechanism. Being partially supported by neutron degeneracy pressure, that by itself could only support Neutron Stars up to $0.75 M_{\odot}$ [4]. In order to keep the core of heavier Neutron Stars from collapsing, interactions between neutrons provided by the strong nuclear force are required. In fact, the interaction terms between the nucleons completely dominate the Equation of State (EoS) of strongly interacting matter.

The outermost structure of a Neutron Star is its "atmosphere", which consists of a plasma of hydrogen and helium nuclei and whose size extends to barely a meter, with most of the plasma being confined to a thin 10cm shell. The latest evidence points to matter at the surface of the Neutron Star being confined to a solid lattice of ordinary atomic nuclei which allows free electrons to "flow" through its gaps. Beneath it, we find the outer crust of the Neutron Star, being made up of a degenerate Fermi Gas of electrons and atomic nuclei - mostly iron being left from before the supernova. With increasing density, electrons and protons undergo electron capture processes and thus nuclei become increasingly neutron-rich. At some point, nuclei are so neutron-rich that the neutrons escape the nuclei, resulting in a free neutron-gas filling the ever decreasing gap between nuclei. This effect is known as "neutron-drip". Since neutrons are fermions, at these densities neutron-degeneracy pressure plays the main role in preventing the collapse of the Neutron Star. Arriving at the core, due to the extreme densities nuclei become so close that nucleons are simultaneously subjected to attraction due to the strong nuclear force, and repulsion due to the coulomb force. This nuclear tug-of-war leads to the formation of exotic structures usually refered to as nuclear pasta. Lastly, the state of matter present in the inner core is still subject of scientific debate. Different models have been put forth, like the presence of quark matter inside the core [5] or the existence of hyperons, particles that - like nucleons - consist of three quarks but include strange quarks. This still present uncertainty is rooted in our lack of knowledge of the EoS at high densities and forces us to come up with different methods to describe the EoS in the denser regions.

Typical Neutron Star radii range from $10 - 13$ km [6, 7], while the mass usually resides between $1 - 2 M_{\odot}$ [8, 9]. A broad discussion about Neutron Stars can be found in [10]. Since the immense densities that are realized inside Neutron Stars cannot be mimicked or reproduced in artificial laboratories, the study of Neutron Stars provides unique information about the Equation of State of strongly interacting matter, about which our knowledge is still limited. The Equation of State is a relation between the energy density and the pressure. In general, it also depends on other properties like temperature, electron fraction, magnetic and electric fields. However, we can approximate Neutron Stars as cold zero-temperature objects since their temperature is low relative to temperatures usually present in high-energy astrophysics. Right after formation through a supernova, a Neutron Star can have sizeable temperatures ∼10MeV. As already explained, this thermal energy gets radiated away quickly through neutrinos to temperatures of order keV. Temperatures of this order of magnitude are regarded cool in Neutron Stars, because the relevant microscopic scale is the deconfinement scale in QCD which is about 150MeV. The Neutron Stars we usually observe are typically very old which means they are already cool [11].

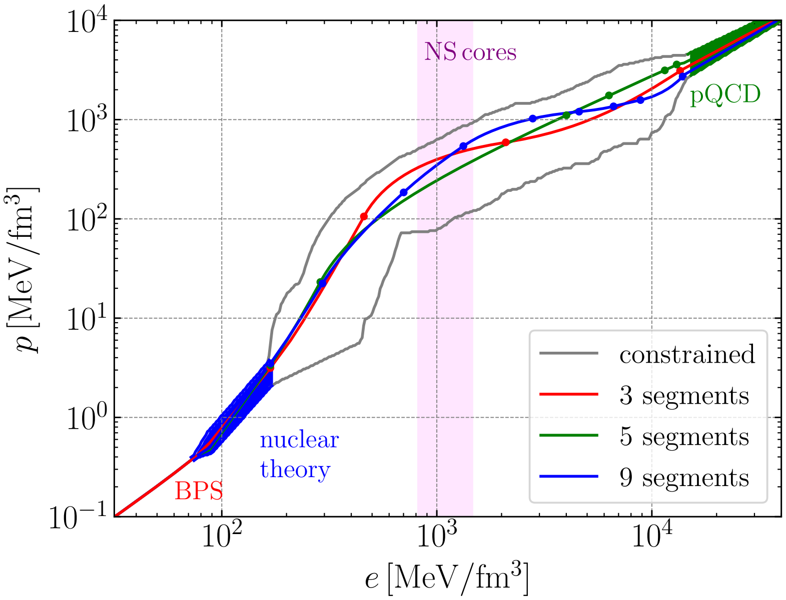

Figure 1: The EoS at intermediate densities is unknown but constrained by the nuclear matter and pQCD EoS.

Ideally, the Equation of State can be extracted from the underlying microscopic theory. When the density is below nuclear saturation density, Chiral Effective Field-Theory (CET) can be used to determine the nuclear matter Equation of State within relatively good accuracy, where the latter stems from uncertainties of the low-energy coupling constants of CET [12]. For very high densities, the theoretical framework of perturbative QCD (pQCD) can be used to derive the Equation of State from microscopic calculations [13]. These calculations apply at densities higher than $40n_s$, much higher than densities that are physically realized inside Neutron Stars and are also afflicted by theoretical uncertainties due to the uncertainty of the renormalization scale parameter of pQCD. Yet, both the pQCD and CET part of the Equation of State play an important role in constraining the overall shape of the Neutron Star Equation of State, which is still unknown in the intermediate densities inbetween the CET and pQCD regimes as is depicted in Fig. 1.

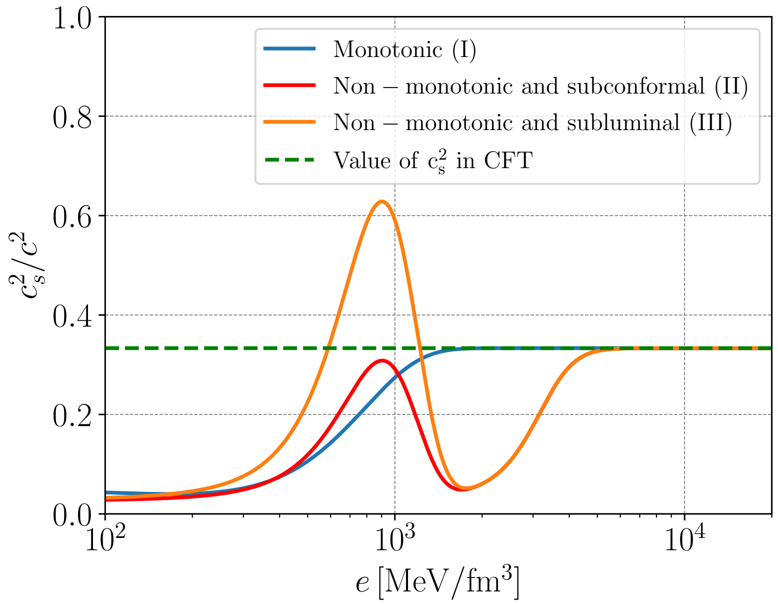

Figure 2: A showcase of the three main classes of c_s^2 profiles using the analytical parametrizations of [14] and [15]. All models converge to 1/3 from below in the high density limit.

The lack of first-principle tools to determine the EoS at densities (1.1-40)n_s forces us to come up with models to parametrize the Equation of State in these regimes. During the last years, several models have been put forth. In this thesis, we will use the speed-of-sound-interpolation method, which has been first introduced by Annala et. al in 2019 [5] and which exploits the relationship between the Equation of State and the speed of sound given by $\frac{dp}{de}c^2 = c_s^2$. This shows, that any Equation of State $p(e)$ corresponds to a speed of sound profile $c_s(e)$. According to pQCD calculations, the speed of sound has to converge to $c_s = \frac{c}{\sqrt{3}}$ - from now on referred to as the conformal value - in the asymptotic high-density limit from below [16]. The behaviour of the speed of sound in the intermediate densities is unknown however, e.g. if it temporarily exceeds the conformal value and thus exhibits a local maximum or if instead it is monotonic. This open debate is depicted in Fig. 2, showing the three most logical sets one can decompose c_s^2 models into. Specifically, monotonic and subconformal $c_s^2 < 1/3$ (I), non-monotonic and subconformal $c_s^2 < 1/3$ (II), non-monotonic and sub-luminal $c_s^2 \leq 1$. Several arguments have been put forth that suggest a universal bound $c_s^2 < 1/3$ [17, 18], favouring scenarios (I) and (II). However, a number of counter examples to this bound are known in QCD at large isospin density [19], two-color QCD [20], quarkyonic matter [21–23], models for high-density QCD [24, 25] and models based on the gauge/ravity duality [26–28]. All of these examples favour scenario (III). Finally, astrophysical measurements of neutron-star masses $\gtrsim 2M_\odot$ [29–31],and theoretical predictions on the maximum gravitational mass [32–34] suggest stiff EoSs with $c_s^2 \gtrsim 1/3$ at densities $\gtrsim n_0$, again favouring scenario (III). Due to the correspondence between $c_s(e)$ and $p(e)$, a better understanding about the behaviour of the speed of sound ultimately leads to a better understanding of the EoS.

The goal of this thesis is to generate a large set of EoSs that by construction satisfy the known theoretical boundary conditions, apply observational constraints onto them and analyze the solutions that satisfy these constraints. We especially pay focus on the properties of the viable speed of sound profiles in terms of monotonicity. For densities below $1.1n_s$ we will use a monotrope (See Chapter 2.1) that is fitted inbetween the "soft" and "stiff" CET EoS of [12], shown in blue in Fig. 1. For densities $\gtrsim 40n_s$ corresponding to baryon chemical potentials ≥ 2.6 GeV we use the analytical parametrization of the pQCD EoS by [13], depicted as the green band in Fig. 1. Since all $c_s(e)$ profiles satisfy $0 \leq c_s^2 = \frac{dp}{de} c^2 \leq 1$ by construction, it is ensured that all EoSs are causal and thermodyamically stable, which are the only theoretical constraints for the intermediate densities.

Furthermore, we will discard any EoS that is unable to support $2M_\odot$ stars as this is the lower uncertainty bound of the mass measurement of PSR J0740+6620 with a mass of $2.08 \pm 0.07 M_\odot$ (68% credible interval) which is the highest Neutron Star mass ever measured [35]. This will result in very "stiff" EoSs that exhibit a rapidly rising c_s. Lastly, all EoSs must satisfy the LIGO/Virgo 90% credible interval for the tidal deformability Λ due to the GW170817 event [36] which we check by imposing the binary-tidal-deformability constraint $\tilde{\Lambda} < 720$ corresponding to the low spin priors $|\chi| < 0.05$ of [1]. This constraint will result in the exclusion of stellar solutions with high radii, because $\Lambda \propto R^5$

1.2 Mass and Radius of Static Neutron Stars

The theoretical backbone of this thesis is the computation of the macroscopic properties of Neutron Stars, i.e. their masses and radii. To accomplish this, we have to solve the Einstein field equations (The convention G = c = 1 will be used throughout this thesis afterwards)

$$R_{\mu\nu} - \frac{1}{2}Rg_{\mu\nu} = \frac{8\pi G}{c^4}T_{\mu\nu}\,, \tag{1}$$

by assuming that the Neutron Star is static, spherically symmetric, isotropic, non-rotating and that its matter can be described as an ideal fluid in hydrostatic equilibrium with a non-trivial Energy-Momentum tensor. Using these assumptions, the Einstein field equations simplify into the so called "Tolman-Oppenheimer-Volkoff" (TOV) equations which can be derived as follows:

The metric tensor of a spherically symmetric, static fluid is given by

$$ds^2 = -e^{2\alpha(r)}dt^2 + e^{2\beta(r)}dr^2 + r^2d\theta^2 + r^2sin^2(\theta)d\phi^2\,. \tag{2}$$

Due to Birkhoffs theorem which states that a spherically symmetric solution of the vacuum Einstein field equations is uniquely described by the Schwarzschild metric, we construct (2) so that it is continuously matched to the Schwarzschild metric at the surface of the star. Taking isotropy, time-independence and spherical symmetry into account, the stress energy-tensor can be expressed as

$$T^{\mu}_{\ \nu} = diag(-e(r), p(r), p(r), p(r))\,, \tag{3}$$

where e(r) is the energy density and p(r) the pressure. Contracting the energy-momentum tensor and computing the Einstein field equations for the given metric yields

$$\frac{1}{r^2}e^{2(\alpha-\beta)}[2\beta' r - (1-e^{2\beta})] = 8\pi e^{2\alpha}e(r)\,, \tag{4}$$

$$\frac{2}{r}\alpha' + \frac{1}{r^2}(1-e^{2\beta}) = 8\pi e^{2\beta}p(r)\,, \tag{5}$$

where the prime denotes partial radial derivatives. Defining the gravitational mass

$$m(r) = 4\pi\int_0^r e(r')r'^2\,dr'\,, \tag{6}$$

which is the mass contained inside a sphere of radius r measured by a distant observer, and integrating (4) one can obtain an expression for the first metric function β

$$e^{-2\beta(r)} = 1 - \frac{2m(r)}{r}\,. \tag{7}$$

Plugging (7) into (5), and rearranging for α' will yield a constraint on the second metric potential

$$\frac{d\alpha(r)}{dr} = \frac{4\pi p r^3 + m}{r(r-2m)} \,. \tag{8}$$

We can arrive at a second equation by exploiting the fact that the covariant derivative of the energy-momentum-tensor vanishes, which is a consequence of the Bianchi-Identities in General Relativity

$$\nabla_\mu T^\mu_\nu = 0 \rightarrow \nabla_\mu T^\mu_r = 0 \,, \tag{9}$$

where only the radial covariant index remains due to the staticity ($\partial_t \rho = \partial_t P = 0$) and isotropy ($\partial_\theta P = \partial_\phi P = 0$) of the problem. Computing (9) and combining with (8) we arrive at the final equations

$$\frac{d\alpha(r)}{dr} = -\frac{1}{p+e}\frac{dp}{dr} \,, \tag{10}$$

$$\frac{dp}{dr} = -\frac{(p+e)(4\pi p r^3 + m)}{r(r-2m)} \,, \tag{11}$$

$$\frac{dm}{dr} = 4\pi e(r) r^2 \,, \tag{12}$$

which are called the TOV equations. In order to solve them one needs to provide a relation between the pressure and the energy density, given by an Equation of State (EoS). For a given Equation of State a family of solutions can be computed by varying the central pressure p_c which is present in the core of the star and serves as a free parameter. The TOV equations will be radially integrated outward until the pressure becomes zero. This way, the radius of the Neutron Star is defined as $p(R) = 0$. In general, equations (10-12) have to be solved numerically which will be explained in detail in Appendix B. The mass of the star can now be computed by

$$M = m(R) = 4\pi \int_0^R e(r') r'^2 \, dr' . \tag{13}$$

Lastly, one could also calculate the baryonic mass M_b which is the total rest mass of the object, neglecting the negative gravitational binding energy

$$M_b = 4\pi \int_0^R \frac{e(r') r'^2}{\sqrt{1 - \frac{2m(r')}{r'}}} dr' \,. \tag{14}$$

In this thesis, ”mass” will always refer to the gravitational mass given by (13). It is worth mentioning that the TOV equations do permit an analytical solution in the case of constant energy density. Although unrealistic, this case still provides a noteable point which becomes visible when looking at the central pressure $p_c = p(r = 0)$ with respect to the mass and radius of a star in this simplified model

$$p_c = \frac{3M}{4\pi R^3}\left[\frac{1-\sqrt{1-2\frac{M}{R}}}{3\sqrt{1-2\frac{M}{R}}-1}\right]. \tag{15}$$

Equation (15) shows not only that the central pressure inside a star depends only on its mass and radius, but also that infinite central pressure would be needed to support a star whose compactness $C = M/R$ approaches 4/9. In a theorem called Buchdals limit [37], it is shown that this critical compactness is even valid for any type of EoSs, showing that $C_{crit} = 4/9$ poses a constraint on any relativistic and compact star. In practice, the compactness for realistic EoS models ranges between 0.1 and 0.2 [38].

2 Constructing Viable Neutron Star EoS Models

2.1 The Piecewise Polytrope Model

The piecewise polytrope model (PP model) is the most common way to parametrize the Neutron Star EoS. Because we will use this model to describe the CET EoS, an introduction of this method is called for. Already discussed thoroughly in [38] and [39], the pressure and rest mass density are related by a simple power law

$$p(\rho) = K\rho^{\Gamma}\,, \tag{16}$$

which is called a monotrope. K is the polytropic constant and Γ is called the adiabatic index. Usually, multiple monotropes are continuosly matched together (polytropes) while varying the remaining free parameters to generate a family of EoSs. In order to obtain the energy density, we consider the first law of thermodynamics

$$d\left(\frac{e}{\rho}\right) = \frac{p}{\rho^2}d\rho\,, \tag{17}$$

which can be integrated to obtain

$$e(\rho) = \rho + \frac{K\rho^{\Gamma}}{\Gamma - 1}\,, \tag{18}$$

where the integration constant has been chosen to ensure that $\lim\limits_{\rho\to 0}\frac{e}{\rho} = 1$. One can now construct piecewise polytropes by ensuring that (17) is satisfied in each segment $\rho_i < \rho < \rho_{i+1}$, which is taken care of by the following parametrizations of pressure and energy density

$$p_i(\rho) = K_i\rho^{\Gamma_i}\,, \tag{19}$$

$$e_i(\rho) = (1 + a_i)\rho + \frac{K_i}{\Gamma_i - 1}\rho^{\Gamma_i}\,. \tag{20}$$

Note how (20) only differs from (18) by the integration constant a_i which takes care of the continuous matching of the energy density. Imposing the continouity of pressure and energy density through $p_i(\rho_i) = p_{i+1}(\rho_i)$ and $e_i(\rho_i) = e_{i+1}(\rho_i)$ yields

$$K_i\rho_i^{\Gamma_i} = K_{i+1}\rho_i^{\Gamma_{i+1}}\,, \tag{21}$$

$$a_{i+1} = \frac{e(\rho_i)}{\rho_i} - 1 - \frac{K_{i+1}}{\Gamma_{i+1} - 1}\rho_i^{\Gamma_{i+1}-1}\,, \tag{22}$$

where $a_0 = 0$ to ensure the low density limit previously discussed. Alternatively one can also directly express the pressure with respect to the energy density

$$p(e) = \kappa e^{\gamma} \,. \tag{23}$$

Here, γ is known as the polytropic index. An advantage of this formulation is that it can easily describe a first order phase transition by setting $\gamma = 0$. In this case, the energy density would stay constant even for increasing pressure. Using the rather interesting thermodynamic relation

$$\Gamma = \gamma + c_s^2 \,, \tag{24}$$

it is easy to check that (16), (23) and (24) yield

$$\Gamma = \frac{\rho}{p}\frac{\partial p}{\partial \rho} = \frac{e+p}{p} c_s^2 \,, \tag{25}$$

$$\gamma = \frac{e}{p}\frac{\partial p}{\partial e} = \frac{e}{p} c_s^2 \,. \tag{26}$$

Another useful relation can be obtained by considering again the first law of thermodynamics

$$dE = TdS - pdV + \mu_B dN \,, \tag{27}$$

where E is the energy, S the entropy and N the baryon number. Transforming these variables into the form of densites like follows

$$e = \frac{E}{V} \qquad s = \frac{S}{M_0} \qquad \rho = \frac{M_0}{V} \,, \tag{28}$$

and now using the conservation of rest mass $dM_0 = 0$ out of which $\frac{dV}{V} = -\frac{d\rho}{\rho}$ follows, we can rewrite (27) as

$$de = T\rho ds + \left(\frac{p+e}{n}\right) dn_B \,. \tag{29}$$

This now finally yields the very important thermodynamic relation

$$\mu_B = \left(\frac{\partial e}{\partial n_B}\right)_{S,V} = \frac{p+e}{n} \,, \tag{30}$$

whose validity is not restricted to the use of polytropes and which will be thoroughly used in this thesis too.

2.2 The Speed of Sound Interpolation Method

While the piecewise polytropic approach is quite straightforward, it is not free of disadvantages. For example, it does not provide enough free parameters to ensure continouity of the speed of sound. This has motivated the authors of [5] to develop a method that builds the EoS starting from a parametrization of the speed of sound. This allows us to directly control the behaviour of the speed of sound, which is indispensable for the questions we are pursuing in this work - concretely, investigating its properties for the subset of solutions that pass theoretical and observational constraints.

We start by parametrizing the squared speed of sound as a linear interpolation between N_p points of $(c^2_{s,i}, \mu_i)_0^{N_p-1}$ where $i \in [0, N_p - 1]$, $c^2_{s,i} \in [0, c^2_{s,max}]$, $c^2_{s,max} \in [0, 1]$ and $\mu_i \in [\mu_{CET}, 2.6 \ \text{GeV}]$. The matching chemical potential μ_{CET} is different for each EoS candidate and given by the CET EoS described in Chapter 2.3. By sampling first the maximum speed of sound, we avoid the fact that subconformal and thus also monotonic solutions are surpressed when $N_p \gg 1$. This happens, because for subconformal solutions to be generated all speed of sound interpolants would have to end up $< 1/3$ simultaneously.

$$c_s^2(\mu_B) = \frac{(\mu_{i+1} - \mu_B)\, c^2_{s,i} + (\mu_B - \mu_i)\, c^2_{s,i+1}}{\mu_{i+1} - \mu_i} \qquad \mu_i \le \mu_B \le \mu_{i+1} \qquad (31)$$

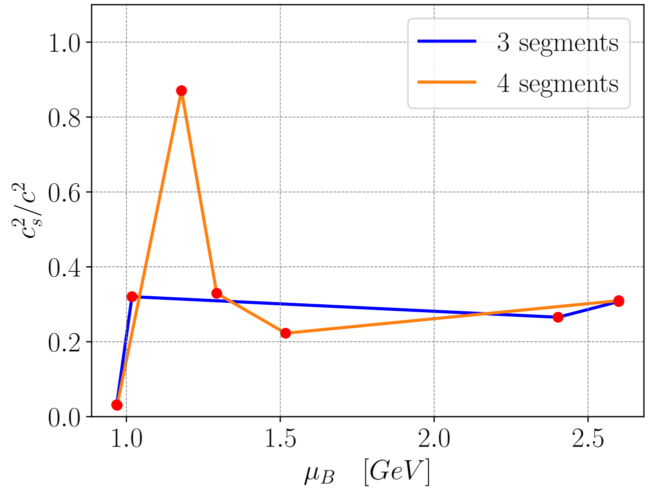

Figure 3: Two examplatory c_s^2 profiles using (31) for 3 and 4 segments. The 3 segment profile is subconformal and both are non-monotonic.

We now seek expressions for the baryon number density $n_B(\mu)$ and the pressure $p(\mu)$. For that, we first differentiate (30) and use (25) to show

$$\frac{d\mu_B}{dn_B} = \frac{\mu_B}{n_B} c_s^2 \,. \tag{32}$$

This differential equation can be easily solved for the baryon density through

$$n_B(\mu_B) = n_{CET}\, exp\left[\int_{\mu_{CET}}^{\mu_B} \frac{d\mu'}{\mu' c_s^2(\mu')}\right] \,, \tag{33}$$

which can be evaluated analytically to yield the baryon density in the i-th segment

$$n_B(\mu_B) = n_{CET} \prod_{k=0}^{i-1} \left(\frac{\mu_k c_{s,k+1}^2}{\mu_{k+1} c_{s,k}^2}\right)^{a_{k,0}} \left[\frac{\mu_i}{\mu_B} \frac{(\mu_{i+1}-\mu_B)c_{s,i}^2 + (\mu_B - \mu_i)c_{s,i+1}^2}{(\mu_{i+1}-\mu_i)c_{s,i}^2}\right]^{a_{i,0}} \,, \tag{34}$$

where the product sign will be ignored for i = 0 and the exponents are defined as

$$a_{i,j} \coloneqq \frac{\mu_{i+1} - \mu_i}{(c_{s,i+1}^2 + j)\mu_i - (c_{s,i}^2 + j)\mu_{i+1}} \,. \tag{35}$$

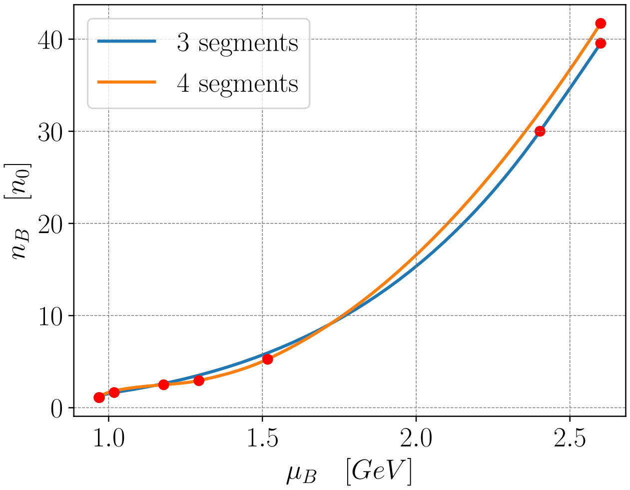

Figure 4: The resulting baryon densities when plugging the two c_s^2 profiles from Fig. 3 into (34)

Note how (32) ensures that by construction the baryon density is not only continuous but also smooth at the transition points - independent of the choice of the interpolation points which can be nicely seen in Fig. 4. The density at the CET matching point is given by n_{CET} which we set as $1.1n_0$. Differentiating (30) again we can arrive at the differential equation

$$\frac{dp}{d\mu_B} = n_B(\mu_B)\,, \tag{36}$$

which can be easily integrated to yield the pressure

$$p(\mu_B) = p_{CET} + \int_{\mu_{CET}}^{\mu_B} d\mu' n_B(\mu')\,, \tag{37}$$

where p_{CET} is the pressure at the CET matching point. Although more complicated, this integral still yields an analytical solution for the pressure

$$\begin{aligned} p(\mu_B) = p_{CET} + \sum_{k=0}^{i-1} a_{k,1}\Bigg[& c_k\,\mu_k\,n(\mu_k)\,{}_2F_1\left(1, 2, \frac{2+a_{k,1}}{1+a_{k,1}}; \frac{(c_k - c_{k+1})\mu_k}{c_k\mu_{k+1} - c_{k+1}\mu_k}\right) \\ & - c_{k+1}\,\mu_{k+1}\,n(\mu_{k+1})\,{}_2F_1\left(1, 2, \frac{2+a_{k,1}}{1+a_{k,1}}; \frac{(c_k - c_{k+1})\mu_{k+1}}{c_k\mu_{k+1} - c_{k+1}\mu_k}\right)\Bigg] \\ & + \frac{\mu\,n(\mu)\,(c_{i+1}(\mu_i - \mu) + c_i(\mu - \mu_{i+1}))\,{}_2F_1\left(1, 2, \frac{2+a_{i,1}}{1+a_{i,1}}; \frac{(c_i - c_{i+1})\mu}{c_i\mu_{i+1} - c_{i+1}\mu_i}\right)}{(1 + c_{i+1})\mu_i - (c_i + 1)\mu_{i+1}} \\ & + a_{i,0}\,c_i\,\mu_i\,n(\mu_i)\,{}_2F_1\left(1, 2, \frac{2+a_{i,1}}{1+a_{i,1}}; \frac{(c_i - c_{i+1})\mu_i}{c_i\mu_{i+1} - c_{i+1}\mu_i}\right)\,. \end{aligned} \tag{38}$$

${}_2F_1$ denotes the hypergeometric function which in general returns complex values and can be evaluated using series or integral representations [40]. Note how in (38), only differences of hypergeometric functions occur which leads to the cancelling of the imaginary parts and so in practice, the pressure will only obtain real values. Finally, using (30) we can now numerically express the actual Equation of State as the pressure with respect to the energy density as displayed in Fig. 6

Since the baryon density (34) is continuous and smooth at the transition points, (36) ensures that this by construction is also true for the pressure. The integration constants n_{CET} and p_{CET} ensure that both thermodynamic quantities are matched to the CET band. It is not guaranteed however, that the pressure, baryon density and c_s^2 satisfy the correct pQCD boundary conditions at $\mu_B = 2.6$ GeV which only happens for specific choices of the interpolants (31). In order to ensure that our EoSs satisfy the pQCD boundary conditions, we agnostically and uniformly sample all interpolants as explained in the beginning of this chapter, except for the first and final ones and keep them if they yield the correct pQCD boundary conditions by chance. The pQCD boundary conditions are discussed in Chapter 2.4.

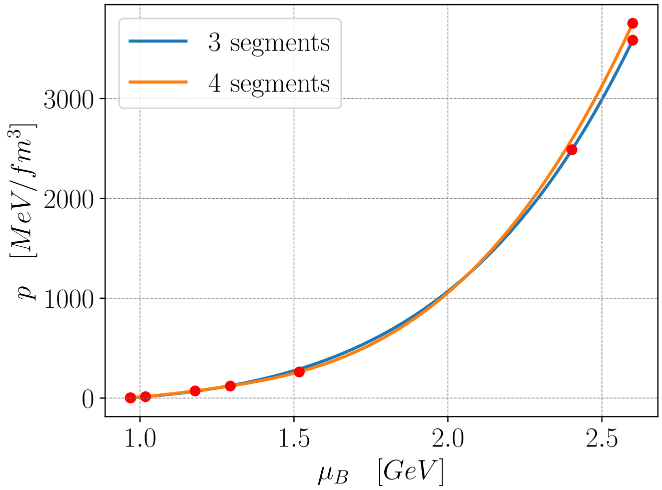

Figure 5: The two pressure profiles resulting from the integration of the previously determined baryon densities (37). As explained above, different to the baryon density the pressure at the pQCD limit lies inside a band spanned by the renormalization scale parameter X, explaining why both curves take on different values in this limit.

When using N_p interpolation points, we have $N_p - 2$ free parameters respectively for $c_{s,i}^2$ and μ_i because the first and final interpolation pairs are fixed by the CET and pQCD constraints. The two constraints for the baryon density and pressure at 2.6 GeV eliminate two further parameters, leaving us with $2N_p - 6$ free parameters. An advantage of this method in contrast to the piecewise polytropes is, that it has less free parameters and is thus more cost-effective. Lastly, by constructing an EoS starting from the speed of sound, continouity and subluminality of the speed of sound are ensured by construction - which is not the case for the piecewise polytropes and a known issue of this method. We close the discussion of the method by noting that although we do not pay particular attention to phase transitions, the method naturally generates EoSs with phase transitions too since sometimes the squared speed of sound will be sampled near zero by chance.

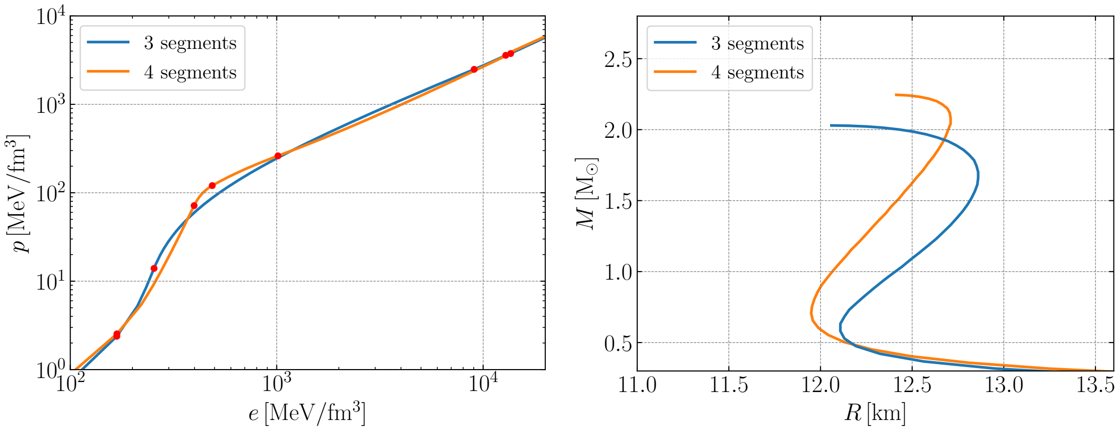

Figure 6: Plugging these EoSs into the TOV equations yields the M-R relation.

2.3 Low-Density EoS from Nuclear Theory

As discussed in the introduction, for densities $n_B \leq 1.1n_0$ the necessity to use an interpolation scheme is not given, since at these small densities effective models constrained by nuclear experiments can be used to compute the EoS with relatively low uncertainty. Using chiral effective theory (CET), one can compute the low-density EoS by using microscopic calculations. The CET EoS we implement is the one introduced by [12] whose microscopic calculations are based on chiral two-neutron and three-neutron interactions. The still present theoretical uncertainty for the neutron matter EoS is mostly due to uncertainties in the low-energy coupling constants of CET. For densities below $n_B \leq 0.5n_0$ we use the Baym-Pethick-Sutherland (BPS) Crust EoS of [41]. For $0.5n_0 \leq n_B \leq 1.1n_0$ we use a monotrope that is fitted in such a way that it matches the CET EoS band provided by the ”soft” and ”stiff” EoSs in Table 5 of [12]. The authors report that their results are not highly sensitive to the upper bound of $1.1n_0$ but state that this is upper bound is most reasonable with respect to the growing uncertainty. Using (16), our monotrope is of the form

$$P(n_B) = p_{trans}\left(\frac{n_B}{n_{trans}}\right)^{\Gamma} . \tag{39}$$

The energy density can be computed from (20)

$$e(n_B) = \left(e_{trans} - \frac{p_{trans}}{\Gamma - 1}\right)\frac{n_B}{n_{trans}} + \frac{p_{trans}\left(\frac{n_B}{n_{trans}}\right)^{\Gamma}}{\Gamma - 1} . \tag{40}$$

The index "trans" refers to the first interpolation point provided in Table 5 of [12] which is matched to the last interpolation point of the BPS - Crust EoS. The following values provide a tight fit to the uncertainty band of [12]:

$$e_{trans} = 87.94\,\mathrm{MeV/fm^3} \quad \mathrm{n_{trans}} = 0.5792\mathrm{n_0}\,, \tag{41}$$

$$p_{trans} \in [0.447, 0.696]\,\mathrm{MeV/fm^3} \quad \Gamma \in [1.76792, 3.2267]\,. \tag{42}$$

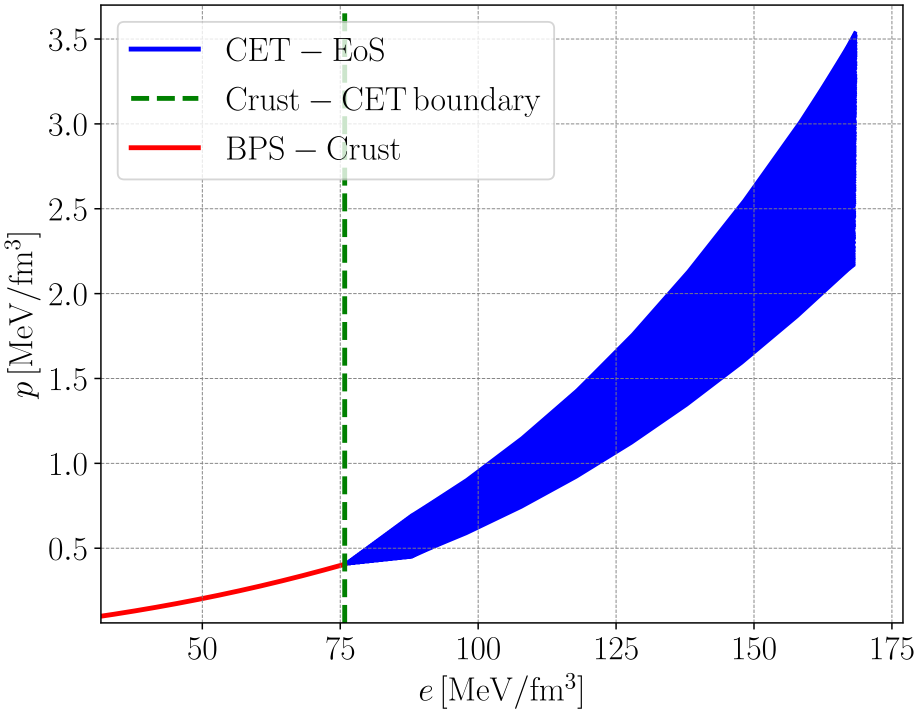

Figure 7: Red: The BPS - Crust EoS by Baym et. al [41]. Blue: The CET EoS provided by a monotrope that is fitted to reside inside the "soft" and "stiff" EoS of [12]. The transition of both EoSs is at e = 87.94 MeV/fm^3

Lastly, we also compute the speed of sound of the CET EoS through numerical differentiation. This then yields the first interpolant of the speed of sound sampling defined by $c_{s,0}^2$ and μ_{CET}, where the latter of which can be computed from (25) and (30).

2.4 High-Density EoS from Perturbative QCD

When the energy density gets very large, an effect called "asymptotic freedom" takes place. Asymptotic freedom means that the coupling constants which describe quark interactions decrease with increasing energy, leading to quarks behaving like free particles in the asymptotic limit. This is good news, because when the coupling constants are low, perturbative calculations become valid and allow to determine the quark matter EoS with relatively good accuracy, thus usually labeled the pQCD EoS. Perturbative results that are computed to a finite order in the coupling constants are dependent of an unphysical parameter, here called X which describes the scale of the chosen renormalization scheme. Thus, X is a way to quantize our ignorance due to the yet undetermined orders and so it decreases with every order that is computed. In an analysis conducted by Fraga et. al [42] it has been shown that the numerical EoS derived by Kurkela et. al [43] can be cast into the form of a simple analytical fit function of the pressure P with respect to the baryon chemical potential μ_B. It describes the pQCD EoS of cold quark matter in β equilibrium and has the form

$$P(\mu_B) = \frac{3}{4\pi^2}\left(\frac{\mu_B}{3}\right)^4 \left(c_1 - \frac{d_1 X^{-\nu_1}}{\mu_B/GeV - d_2 X^{-\nu_2}}\right) . \tag{43}$$

The authors report that the fitting is optimal for the following values of the fitting parameters in the regime below $\mu_B < 6$ GeV

$$c_1 = 0.9008 \quad d_1 = 0.5034 \quad d_2 = 1.452 \quad \nu_1 = 0.3553 \quad \nu_2 = 0.9101 . \tag{44}$$

Using (36) and (42) we can compute the energy density

$$e(\mu_B) = -P(\mu_B) + \frac{\mu_B^4}{27\pi^2}\left(c_1 - \frac{d_1}{X^{\nu_1}\left(\mu_B - \frac{d_2}{X^{-\nu_2}}\right)}\right) + \frac{d_1 \mu_B^5}{108\pi^2 X^{\nu_1}\left(\mu_B - \frac{d_2}{X^{\nu_2}}\right)^2} . \tag{45}$$

The question arises where we attach this pQCD EoS to the part of the EoS that comes from the speed-of-sound interpolation method. The authors of [43] report that the relative uncertainty of the quark matter EoS at 2.6 GeV is the same as the uncertainty of the CET EoS at $1.1 n_0$, marking 2.6 GeV as the attachment point. Since the pressure of the pQCD EoS (43) at the transition point is dependent on X only, we ensure the matching by choosing X in such a way that (43) has the same pressure value as the one coming from the speed of sound interpolation EoS.

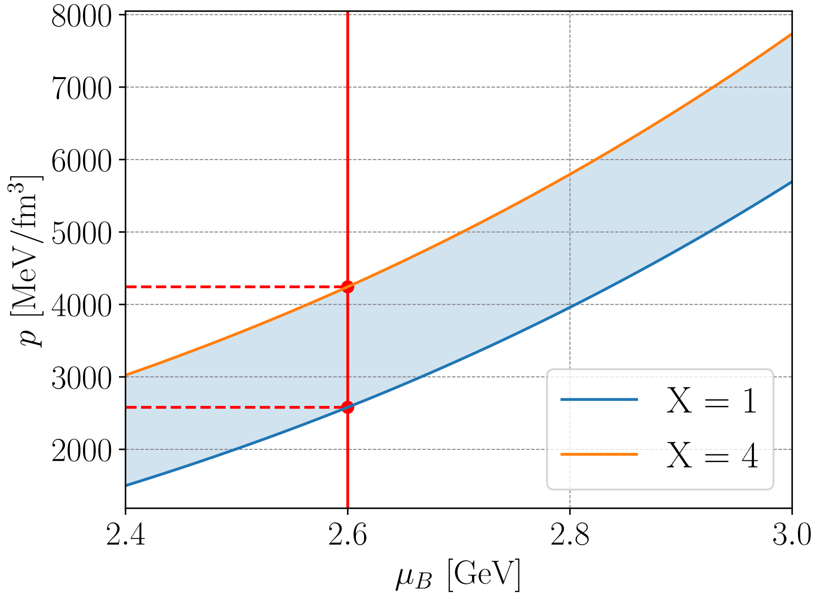

Figure 8: The fitting function (45), showing the upper and lower uncertainty bounds corresponding to X = {1,4}. The two dashed lines show the upper and lower pressure bound at $\mu_B = 2.6$ GeV corresponding to the interval 2580-4243 MeV/fm^3 which marks the interval that all EoSs coming from the speed-of-sound interpolation arrive at.

Through formulae (43) and (45), one can also analytically compute the speed of sound of the pQCD EoS given by

$$c_s^2 = \frac{dp}{de} = \frac{dp}{d\mu_B}\left[\frac{de}{d\mu_B}\right]^{-1} . \tag{46}$$

The speed of sound profile of every EoS we generate is ensured to be matched continuously to the pQCD speed of sound dictated by (46). Since the pressure is also continuous this means that all EoSs are smooth and continuous by construction. While the CET EoS provides the first interpolant of the speed of sound interpolation method, the pQCD EoS now provides the last interpolation point, given by (46) and $\mu_{pQCD} = 2.6$ GeV. In practice, it turns out that (46) yields $c_s^2(\mu_B = 2.6 \text{ GeV}) \lesssim 1/3$. This is not a coincidence however and an important point which will be elaborated on at the end of this chapter. As explained in the beginning of this chapter, QCD becomes asymptotically free in the high energy limit.

Secondly, in this limit and when using 4 dimensions, the ground state of QCD becomes conformally invariant [44]. Given that scale invariance follows out of conformal symmetry, anything that would define a unique energyscale has to vanish. As a consequence, one can impose that the trace of the energy-momentum tensor (3) vanishes, which is equivalent to

$$p = \frac{1}{3}e \quad \rightarrow \quad \lim_{e\to\infty} c_s^2(e) = \frac{1}{3}\,. \tag{47}$$

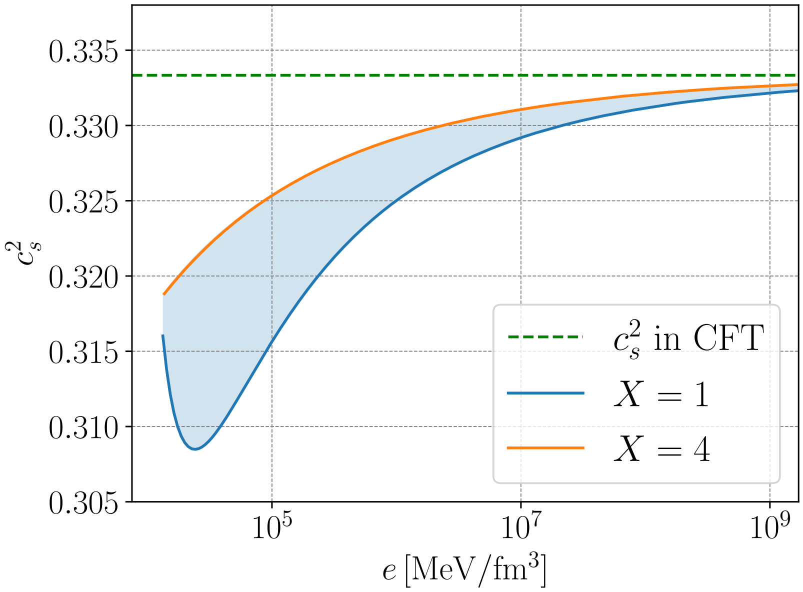

Figure 9: The squared speed of sound (46) such as given by the fit function (43) for the two boundary cases X = 1 (blue) and X = 4 (blue). The curves are truncated on the left at the attachment point $\mu_B = 2.6$. The dashed green line denotes the value of the speed of sound in conformal field theory (CFT).

In Fig. 9 one can see that the fit function (43) takes this ”conformal limit” of the squared speed of sound into account. Additionally, it is visible that the speed of sound converges to this limit from below. It is also noteworthy, that the value of the squared speed of sound at the attachment point $\mu_B = 2.6$ GeV does not exactly yield 1/3 but rather resides slightly below 1/3, since at the corresponding energy density it has not yet converged close enough to 1/3.

3 Observational Constraints on the Neutron Star EoS

3.1 Mass and Radius Constraints by Astrophysical Observations

In the previous chapters, it was thoroughly explained how to construct EoS models that satisfy the known theoretical constraints. In the ongoing endeavour of pinning down the dense matter EoS, it is crucial to conduct astrophysical measurements of Neutron Star properties. This way, one can successively exclude EoSs that are not able to account for the growing observational evidence. In detail, the most relevant measurements that serve this purpose are those of the Neutron Stars mass and radius, as well as its tidal deformability (Chapter 3.2). In the recent years, the NICER experiment onboard the International Space Station provided ongoing mass and radius measurements of Neutron Stars. Several independent groups have analyzed these measurements. While they partly used different methods for obtaining their measurements and also provide different error bars, this chapter is not devoted to the experimental and methodological details. Rather, the relevant numerical values of the measurements are presented and their expected impact on the EoS ensemble briefly discussed.

Neutron Star PSR J0740+6620 is highly likely to be the most massive known Neutron Star. Its mass is reported to be $2.08^{+0.07}_{-0.07}M_{\odot}$ (68.3% credibility) [45]. Comparably to that, the mass of Neutron Star PSR J0348+0432 has been reported to be $2.01^{+0.04}_{-0.04}M_{\odot}$ (68.3 % credibility) [29]. These measurements pose tight constraints to the dense matter EoS since they have to be stiff enough to support a Neutron Star with $2M_{\odot}$. Thus, we will expect a rapid increase of the speed of sound to account for this stiffness. Future mass measurements will only be more constraining if they yield a higher mass than reported by the previous findings.

In addition, there have been two independent measurements of the radius of PSR J0740+6620. One of them reported a radius of $13.7^{+2.6}_{-1.5}$ km (68% credible interval) [45], while the other group reported $12.39^{+1.3}_{-0.98}$ km (16% and 84% quartiles) [46]. Another radius measurement stems from the pulsar PSR J0030+0451. Again, the data of this measurement has been analyzed by two different groups. In [47], the authors report a radius of $12.71^{+1.14}_{-1.19}$ km while stating a mass of $1.34^{+0.15}_{-0.16}M_{\odot}$, corresponding to the 16% and 84% quartiles. The second group reports a radius of $13.02^{+1.24}_{-1.06}$ km with a mass of $1.44^{+0.15}_{-0.14}M_{\odot}$, both corresponding to the 68% credibility interval [48].

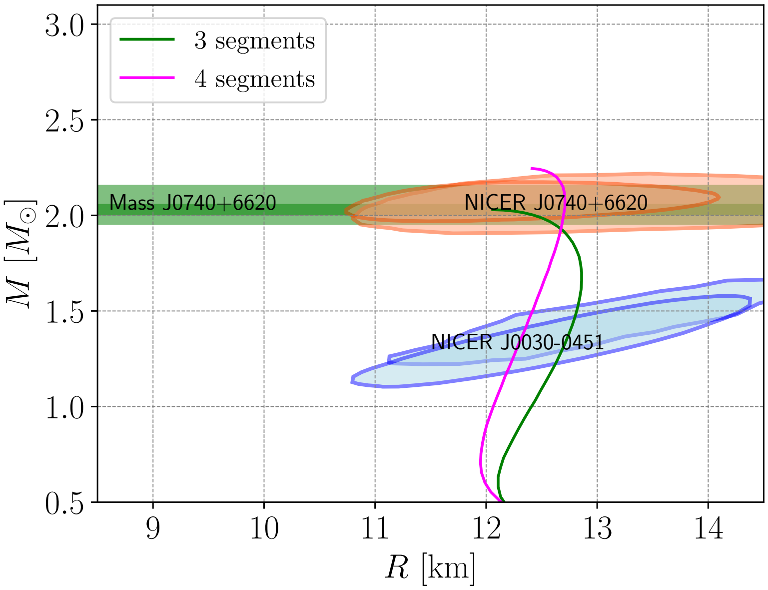

Figure 10: Graphical depiction of the astrophysical NS measurements explained in this chapter. The two orange contours represent the two different measurements of J0740+6620. For the case of J0030+00451, the analogous measurements are shown in blue. The green contours depict the mass measurements of J0740+6620. Lastly, the two MR solutions of Fig. 6 are shown.

For an Equation of State to be in agreement with the astrophysical observations, we demand that its corresponding MR curve passes through each of the contours that are seen in Fig. 10, as this is the case for the two examplatory curves. In practice, an easy way to implement this is by accepting only those EoSs whose MR curve satisfy $R(1.1M_\odot) > 10.8$ km, $R(2.0M_\odot) > 10.75$ km and $M_{TOV} \geq 2.0M_\odot$.

3.2 Constraints on the Tidal Deformability due to GW170817

Besides the experimental mass and radius measurements of Neutron Stars, the tidal deformability can serve as another possibility to constrain the Neutron Star EoS. During the inspiral of two Neutron Stars that are about to merge, gravitational waves are emitted that can be measured and used to draw conclusions about the EoS of Neutron Star matter. The crucial link comes from the tidal distortion the stars are affected by during the inspiral, which influence the gravitational wave signal and can be described by a single parameter Λ, which can be seen as a measurement of how much a Neutron Star deforms in the tidal field of its binary partner.

Mathematically, the tidal deformability can be defined as the proportionality constant of the static external quadrupolar tidal field $\mathcal{E}_{ij}$ and the stars induced quadrupolar moment Q_{ij} [49]. Both of these quantities show up when considering a static, spherically symmetric star located in a tidal field. For large r, the g_{tt} component of the metric in the stars local asymptotic rest frame can be expanded as [50]

$$\frac{1-g_{tt}}{2} = -\frac{M}{r} - \frac{3Q_{ij}}{2r^3}\left(n^i n^j - \frac{1}{3}\delta^{ij}\right) + O\left(\frac{1}{r^3}\right) + \frac{1}{2}\mathcal{E}_{ij}x^i x^j + O\left(r^3\right) \,, \tag{48}$$

where $n^i = \frac{x^i}{r}$. In linear order, the induced quadrupole moment is related to the tidal field by

$$Q_{ij} = -\Lambda \mathcal{E}_{ij} \,, \tag{49}$$

where we meet the tidal deformability Λ for the first time. The tidal deformability can be computed numerically: By introducing a pertubation to the spherically symmetric metric of [49, 50] one can arrive at a set of two separate ODE's of the pertubation H(r) and its derivative β(r)

$$\frac{dH}{dr} = \beta \,, \tag{50}$$

$$\begin{aligned}\frac{d\beta}{dr} &= 2\left(1-2\frac{m}{r}\right)^{-1} H \left\{-2\pi[5e+9p+\frac{de}{dp}(e+p)]\right.\\ &\quad \left. + \frac{3}{r^2} + 2\left(1-2\frac{m}{r}\right)^{-1}\left(\frac{m}{r^2}+4\pi r p\right)^2\right\}\\ &\quad + \frac{2\beta}{r}\left(1-2\frac{m}{r}\right)^{-1}\left\{-1+\frac{m}{r}+2\pi r^2(e-p)\right\} \,.\end{aligned} \tag{51}$$

These two equations are solved simultaneously with the TOV equations (11-12) by radial integration starting from an infinitesimal step outside the center towards the surface of the star. For the initial conditions we use the expansion $H(r) = a_0 r^2$ and $\beta(r) = 2a_0 r$. The constant a_0 determines how much the star can be deformed and can be chosen arbitrarily since it will cancel in the formulae for the tidal deformability. Once the radius of the star has been computed, one can proceed to compute the quantities $y = \frac{R\beta(R)}{H(R)}$ and the compactness $C = \frac{m(R)}{R}$. Now, one has everything to compute the $l = 2$ mode quadrupolar tidal love number k_2 [51]

$$\begin{aligned}k_2 = \frac{8C^5}{5}\left(1-2C\right)^2\left[2+2C(y-1)-y\right]\cdot\{2C\left[6-3y+3C(5y-8)\right]\\ +4C^3\left[13-11y+C(3y-2)+2C^2(1+y)\right]\\ +3\left(1-2C\right)^2\left[2-y+2C(y-1)\right]\ln\left(1-2C\right)\}^{-1}\,,\end{aligned} \tag{52}$$

out of which the tidal deformability ultimately follows through

$$\Lambda = \frac{2}{3}k_2\left(\frac{R}{M}\right)^5 . \tag{53}$$

The phase shift of a gravitational wave signal of two merging Neutron Stars will be affected by the tidal deformabilities of the two stars. The leading tidal contribution to the phase of the gravitational wave depends on a dimensionless mass weighted average of the two different tidal deformabilities $\tilde{\Lambda}$ and is formally of fifth post-Newtonian order [52]

$$\delta\psi = -\frac{117}{256}\frac{\left(\pi M_{tot} f_{GW}\right)^{\frac{5}{3}}}{\mu} M_{tot}\tilde{\Lambda}\,, \tag{54}$$

where $\mu = \frac{m_1 m_2}{M_{tot}^2}$, $M_{tot} = m_1 + m_2$ and f_{GW} is the frequency of the gravitational wave. The mass weighted dimensionless tidal deformability is defined as

$$\tilde{\Lambda} = \frac{16}{13}\frac{\left(12m_2+m_1\right)m_1^4\Lambda_1 + \left(12m_1+m_2\right)m_2^4\Lambda_2}{\left(m_1+m_2\right)^5}\,, \tag{55}$$

which yields $\tilde{\Lambda} = \Lambda_1 = \Lambda_2$ for $m_1 = m_2$. For every EoS, we will compute the corresponding MR curve and all the tidal deformabilities along this curve by using (11),(12) and (53). We now discard an EoS if there isnt at least one pair of stellar solutions (m_1, Λ_1),(m_2, Λ_2) that simultaneously satisfies $q = \frac{m_2}{m_1} > 0.73$, $\mathcal{M}_{chirp} = \frac{(m_1 m_2)^{3/5}}{(m_1+m_2)^{1/5}} = 1.186 M_{\odot}$ and $\tilde{\Lambda} < 720$ [1]. Since the tidal deformability depends heavily on the radius (53), this constraint penalizes solutions with high radii. While there have been multiple gravitational wave detections by the LIGO/Virgo collaboration, GW170817 is the only one that is confirmed to originate from a NS-NS binary beyond any reasonable doubt. Future observations promise even tighter constraints to the dense matter EoS.

4 Results

In this section, we will present the main results of this thesis, out of which parts were published in [53].

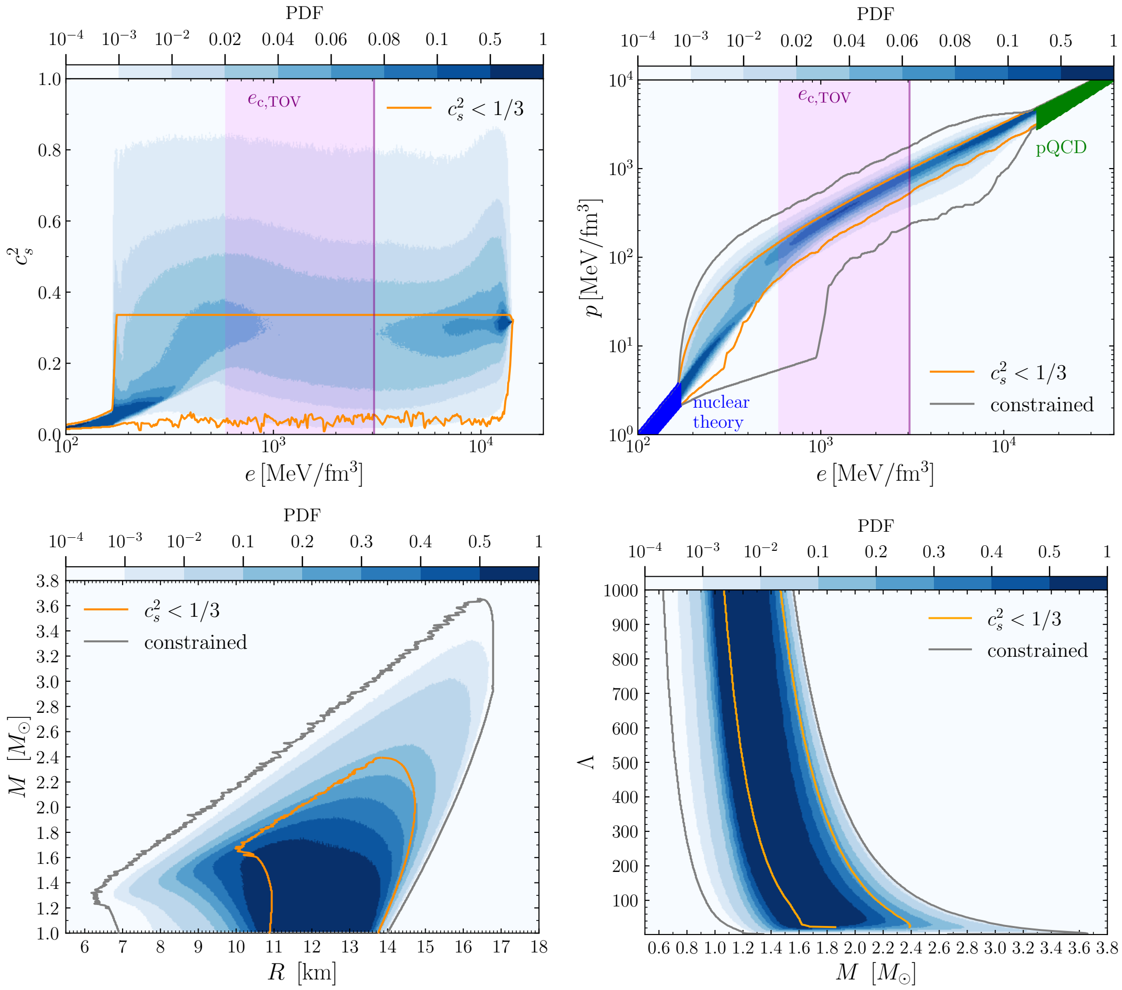

Figure 11: PDF plots of $\sim 10^7$ EoSs using 7 segments without having implemented constraints from astrophysical observations. The yellow contours enclose the subset of subconformal solutions. The purple band marks the 95% credible interval of the maximum central energy density. Top left: Squared speed of sound with respect to the energy density. Top right: Corresponding EoSs. Bottom left: Mass-radius relation. Bottom right: Tidal deformability (53) with respect to the mass.

We start with an unconstrained computation, this means that in this computation, we do not impose any observational, but only the discussed theoretical constraints. For a thorough explanation on how we determine the PDF's we use, we refer the reader to Appendix B. As expected, Fig. 11 shows how our unconstrained ensemble spans a wide range of possible solutions that is highly consistent with similar calculations shown in Fig. 2 of [54]. While the EoS ensemble mostly concentrates on the blue band, the gray contour shows the existence of very soft EoSs which will be discarded once we consider observational data. This plot shows well how theoretical knowledge coming from nuclear theory and pQCD alone can help to constrain the set of possible EoS models. The largest possible Neutron Star mass we can report from this computation is $M_{max} = 3.63 M_{\odot}$. The largest radius $R_{max} = 16.81$ km.

Focusing on the subconformal solutions, as expected, one can see clearly that the largest mass they can support is way less than that of a generic speed of sound profile, yielding $M_{sub,max} = 2.39 M_{\odot}$. The reason for that is due to that a subconformal speed of sound profile yields a softer EoS which is thus unable to support high-mass Neutron Stars. As can be seen in the behaviour of the PDF, it is only a low number of solutions that occupy these large mass and radius regimes though. The cause of that can already been spotted in the speed of sound plot: Only a rare number of solutions obtain $c_s^2 > 0.8$ and are thus not stiff enough to support such huge masses. Furthermore one can see that the theoretical constraints alone predict that a majority of solutions surpasses $c_s^2 > 1/3$ with two visible peaks at $\mathrm{e} \approx 800$ MeV/fm$^{\mathbf{3}}$ and one shortly before the pQCD bound. While the first peak is not a surprise as the stiffening of the EoS plays a big role in producing $> 2 M_{\odot}$ stars, the second peak concerned us.

As explained in Chapter 2.4, pQCD calculations show that in the high energy density limit c_s^2 has to approach to the value in CFT from below. While this is still the case for the subset of solutions responsible for this second peak, it is unexpected that the speed of sound is strongly fluctuating where it should converge. Moreover such large fluctuations on a small energy scale would mean rapid changes in material properties which seems unnatural. Given that this limit is derived from microscopic calculations, the objection that these solutions will be erased once imposing the astrophysical observations is untenable. Thus, in Fig. 12 it can be seen that this peak is still present even after imposing the additional constraints. The cause of this second peak is that the freedom of sampling c_s^2 and μ agnostically simply allows for exotic solutions like that. In Appendix B we investigate the impact that an artificial constraint has in eliminating such strongly fluctuating solutions. In the bottom right panel we show the tidal deformability (53) with respect to the mass.

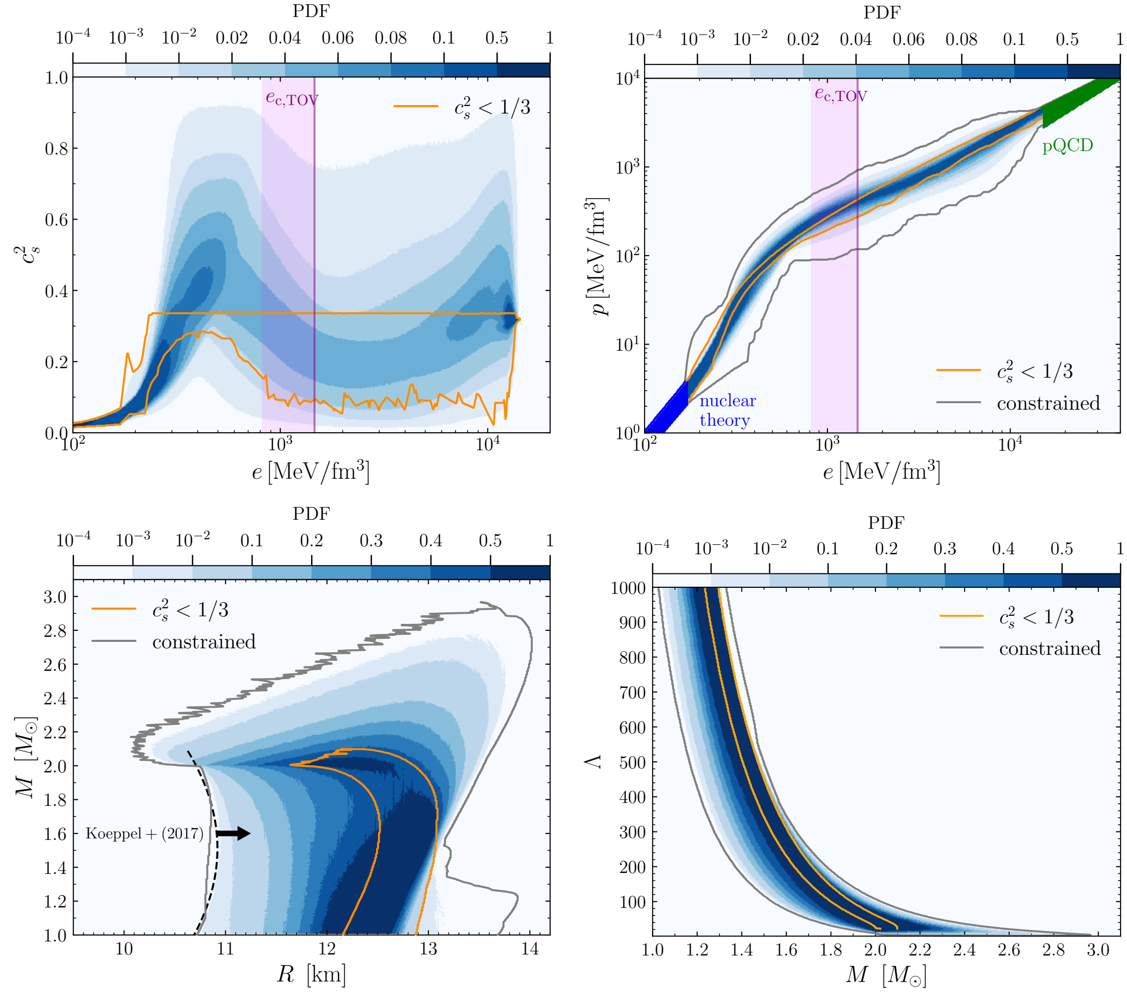

Figure 12: The same plots as in Fig. 11 but now considering astrophysical observations. Shown are all $\sim 10^6$ EoSs that yield $M_{TOV} \geq 2M_\odot$ and who are in accordance with the mass and radius measurements of PSR J0740+6620 and PSR J0030+0451 - implemented as R($1.1M_\odot$) > 10.8 km and R($2.0M_\odot$) > 10.75 km. Lastly we demand that $\tilde{\Lambda} < 720$ for at least one stellar model per EoS with $\mathcal{M}_{chirp} = 1.186M_\odot$ and $\frac{m_2}{m_1} > 0.73$.

As the tidal deformability is heavily linked with astrophysical observations this plot isn't very telling when only considering theoretical constraints. In Fig. 12 we present the main result of this thesis as they display the set of all viable stellar models that are in accordance with the known astronomical data. Given that this thesis is about the speed of sound in Neutron Stars, the top left plot is of prime interest. Interestingly, the speed of sound obeys a steep rise towards $c_s^2 \gtrsim 1/3$ below e $\lesssim$ 500 MeV/fm$^{\mathbf{3}}$ corresponding to a stiffening of the EoS at these densities. The vast majority of solutions then exceed the conformal value of 1/3 to form the still present peak at intermediate densities. Most models containing quarkyonic matter feature a peak at low densities show such a peak [21]. The subsequent decrease most solutions then follow ultimately culminates in the unnatural second peak already discussed. The yellow contour shows the subset of subconformal solution that never exceed $c_s^2 >$ 1/3. In the smaller energy densities they reveal a lower bound of $c_s^2 \gtrsim 0.2$. This explains an observation that will be discussed in Fig. 15, namely that the number of subconformal solutions is low with respect to the whole sample ($\sim 0.001\%$) as their successfull sampling has to satisfy this additional geometrical subtlety. Given that the smallest $e_{c,TOV}$ is way larger than the first peak, this is evidence that this peak is realized in real Neutron Stars.

In the top right we show the corresponding EoS ensemble. Although the outer gray contour of our data is in good agreement with [54], the distribution encoded in the PDF is new. Thanks to that one can see that the bulk of curves cluster in an even smaller band than the gray one. The kink that is visible at around e = 700 MeV/fm$^{\mathbf{3}}$ is caused due to the phase transition from hadronic to quarkyonic matter. This so called "deconfined phase transition" is accompanied by a rapid softening of the EoS. Analogous to the phase transition of water from solid to liquid, when the latent heat gets released the pressure increases while the density stays mostly constant. The presence of quark matter cores in Neutron Stars depends on whether the central energy density is reached after or before the deconfined phase transition. While still being subject to debate, in [5] a case for the existence of quark matter cores is made. Furthermore, one can see that the blue band coincides well with the subconformal band except for the region around e $\lesssim$ 500 MeV/fm$^{\mathbf{3}}$. This is interesting, because if we would not have the speed of sound plot we might falsely interpret this as evidence that subconformal solutions are statistically favoured.

In the lower left we see the PDF of the mass radius ensemble. From that, we can pull an upper mass of $M \lesssim 3M_\odot$ as well as a lower limit for the radius of $R \gtrsim 10.5$ km. This fits very well the analytical lower bound R/km $\gtrsim$ -0.88$(M/M_\odot)^{\mathbf{2}}$+2.66$(M/M_\odot)$ + 8.91 of the threshold mass [55]. The same is true for the upper mass limit of the subconformal solutions $M \approx 2.1M_\odot$, being in good agreement with [54] and thus confirming the incompatibility of $M \gtrsim 2M_\odot$ stars and a subconformal EoS. In fact, the measurement of a Neutron Star with $M > 2.1M_\odot$ would exclude the scenario of a subconformal EoS entirely. Interestingly, our computations reproduce the hump at around $M = 2.1M_{\odot}$ also seen in [54]. An independent analysis of the EoSs responsible for this hump concludes that they are actually dyamically unstable [56]. In Fig. 13 we present constant mass slices taken from this PDF for $M = 1.4M_{\odot}$ and $M = 2M_{\odot}$. By determining the respective median and the 95% confidence interval we can come up with the radius estimates $R_{1.4} = 12.42^{+0.52}_{-0.99}$ km and $R_{2.0} = 12.11^{+1.11}_{-1.23}$ km.

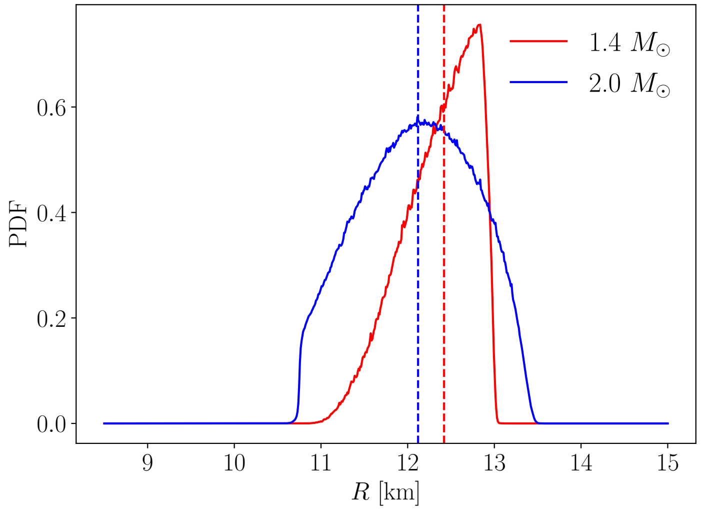

Figure 13: Constant mass slices at $1.4M_{\odot}$ and $2M_{\odot}$ of the MR ensemble shown in Fig. 12. Respective median values are displayed as vertical lines. $R_{1.4} = 12.42^{+0.52}_{-0.99}$ km and $R_{2.0} = 12.11^{+1.11}_{-1.23}$ km.

In contrast to the $2M_{\odot}$ slice, the $1.4M_{\odot}$ slice obeys a rightward skew which is due to the tidal-deformability constraint that penalizes large radii. Even though we are using a different method to generate the EoSs, our median value of $R_{1.4}$ agrees well with the piecewise polytropic results of [57] ($12.00 < R_{1.4} < 13.45$ km) and also within the error bars of [58]. Nearing the end of our agnostic analysis, we shift our focus towards two quantities which are special due to the fact that they can be directly measured from gravitational wave observations and are thus of prime interest. In the differential equations that describe the orbital evolution of a compact binary system, a mathematical term called the "chirp mass" $\mathcal{M}_{chirp} = \frac{(m_1 m_2)^{3/5}}{(m_1+m_2)^{1/5}}$ arises in the leading order contribution. Hence, in gravitational wave observations, it is much easier to measure the chirp mass instead of the two component masses. The interesting thing is that we can relate this relatively easy measureable quantity with another quantity that yields precious information about the microphysics, namely the already introduced binary tidal deformability $\tilde{\Lambda}$. In Fig. 14, we show the relation between the two quantities before and after we impose the observational constraints. Because the gravitational wave event GW170817 had a reported chirp mass of $\mathcal{M}_{chirp} = 1.186 M_{\odot}$, we also provide the distribution of the respective slices as well as the medians. It can be seen that imposing the observational constraints has the expected effect of narrowing down the band. This can also be seen in the

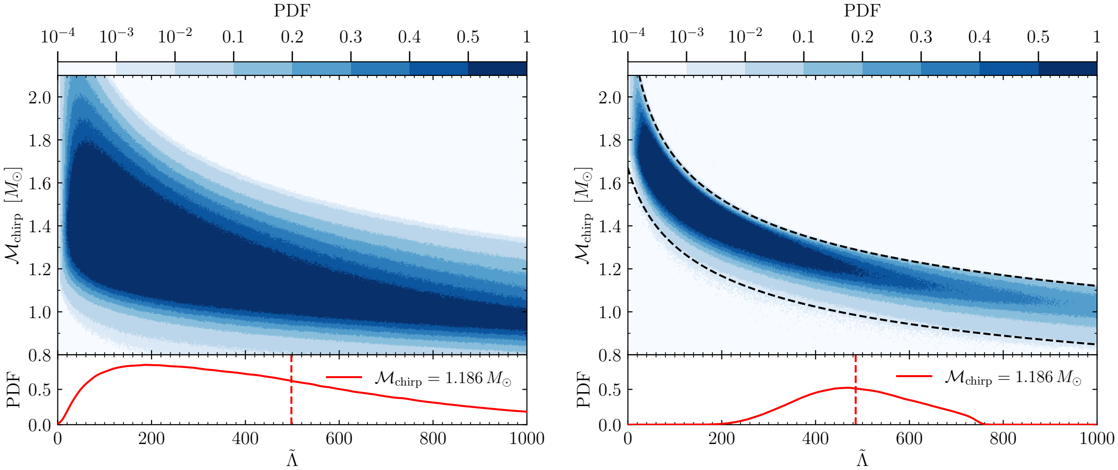

Figure 14: Left: PDF of the chirp mass with respect to the binary tidal deformability before imposing observational constraints. A sliced PDF for $\mathcal{M}_{chirp} = 1.186 M_{\odot}$ is presented with a median of $\tilde{\Lambda}_{1.186} = 498^{+477}_{-474}$. Right: Same plot but having observational constraints included. Dashed lines are analytical fits at a 99% confidence level provided by (56). The median yields $\tilde{\Lambda}_{1.186} = 483^{+224}_{-210}$.

$\mathcal{M}_{chirp}$ slice as it is cut off from the left and right. Interestingly though, the median does not change significantly. Due to the fact that in the right plot of Fig. 14 we are agnostic with respect to the mass ratio, one can still see solutions that have $\tilde{\Lambda} > 720$ for $\mathcal{M}_{chirp} = 1.186 M_{\odot}$. This is no contradiction to the $\tilde{\Lambda} < 720$ constraint of GW180817 since it is only valid for $\frac{m_2}{m_1} > 0.73$. We report a median of $\tilde{\Lambda}_{1.186} = 483^{+224}_{-210}$ at a 95% confidence level for the right plot. While the upper bound is mostly influenced by the $\tilde{\Lambda}$ constraint, the lower bound is of predictive nature. Lastly, we fitted the envelope of the band at a 99% confidence level and provide the following analytical estimate of the minimum (maximum) value of $\tilde{\Lambda}$ as a function of $\mathcal{M}_{chirp}$

$$\tilde{\Lambda}_{min(max)} = a + b\, \mathcal{M}_{chirp}^{c}\,, \tag{56}$$

where a = -50(-20), b = 500(1800) and c = -4.5(-5.0). Thus, (56) provides a fast and direct estimate of the binary tidal deformability of future gravitational wave observations by simply plugging in the measured $\mathcal{M}_{chirp}$. Finally, for the last time in our agnostic analysis we turn our focus to the properties of the speed of sound of the EoSs we generate. In the introduction, it was explained that one can seperate EoSs into three different classes depending on how their corresponding c_s^2 behaves. Given that we started with an initial ensemble of $1.5 \cdot 10^7$ EoSs, we were not only curious about how many of them satisfy the observational constraints, but also how the EoSs are statistically distributed with respect to their sound speed behaviour.

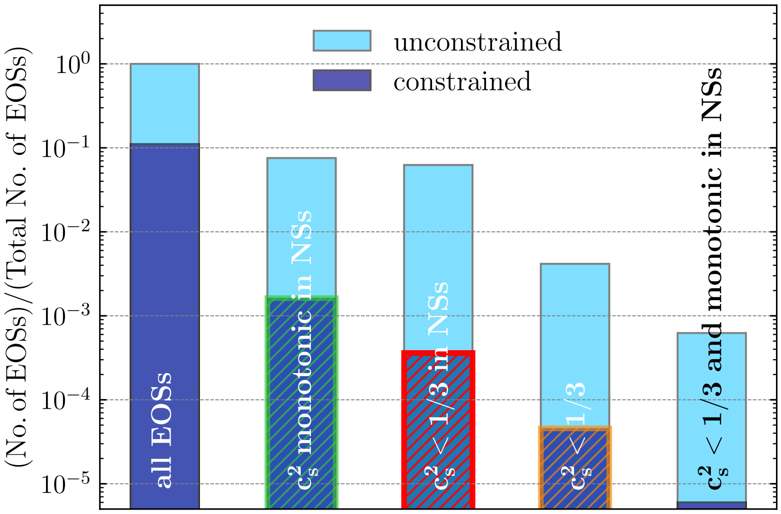

Figure 15: Histogram that shows the most relevant sets we can decompose our EoSs in. We present the statistics before imposing the observational constraints (light blue) and afterwards (dark blue).

The leftmost histogram depicts that out of our $1.5 \cdot 10^7$ EoSs the number of EoSs that survive are reduced by roughly one magnitude, namely $1.7 \cdot 10^6$. The green hatched histogram displays the fraction of EoSs whose c_s^2 profile is either globally monotonic or monotonic until at least $e_{c,TOV}$ and thus monotonic inside the Neutron Star. We apply the same logic to the red hatched set of EoSs whose c_s^2 profile is either globally subconformal or at least up until $e_{c,TOV}$. Here, the subset of constraint-satisfiying EoSs is reduced by two orders of magnitude from $2.5 \cdot 10^5$ to $5.4 \cdot 10^3$ EoSs. The major cause of this suppression is the $M_{TOV} > 2M_\odot$ constraint as it penalizes soft EoSs. Comparably, EoSs with a globally subconformal c_s^2 are reduced by two orders of magnitudes as well to only 684 EoSs (yellow hatched histogram).

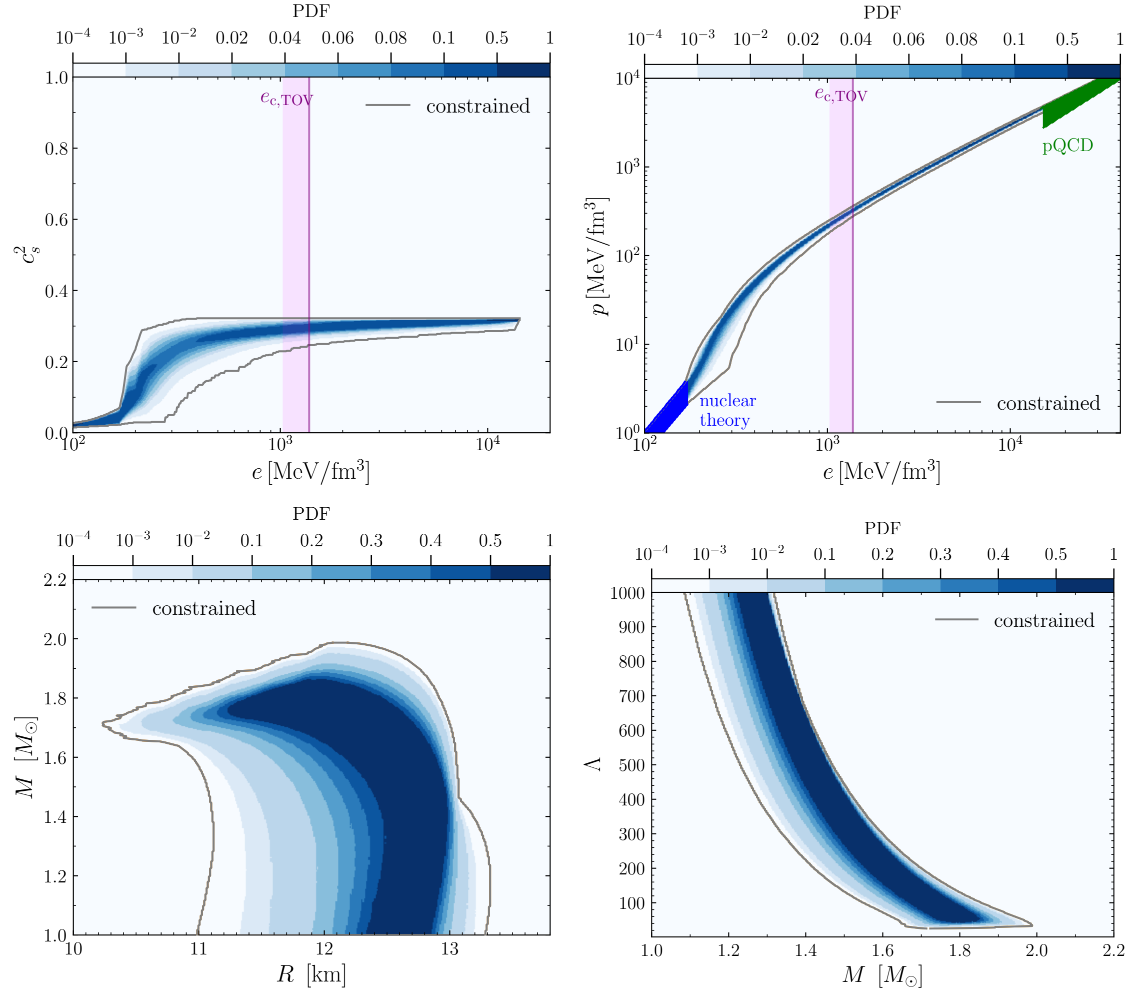

Figure 16: The same plots as in Fig. 12 but only using EoSs whose corresponding speed of sound profile is globally monotonic by construction and thus subconformal by nature. The gray contour is the envelope of the data. Furthermore the only observational constraints imposed are those of GW170817.

The last histogram shows the subset of EoSs who are subconformal and monotonic inside Neutron Stars. With 90 surviving EoSs this is the smallest relevant subset. Interestingly, we do not find a single EoS whose c_s^2 is globally monotonic. Being unsure if there is a physical reason behind this or if this is due to a high statistical suppression, this observation motivated us to conduct a separate biased computation containing only EoSs whose c_s^2 is monotonic by construction. The results of this computation can be seen in Fig. 16. The most interesting plot of those four is the bottom left MR plot as it explains why we did not find any globally monotonic solution in our agnostic ensemble depicted in Fig. 12 and counted in Fig. 15. It turns out that an EoS with a globally monotonic speed of sound is apparently not stiff enough to support a $2M_\odot$ Neutron Star and is thus most likely ruled out by the mass measurement of PSR J0740+6620. Indeed, the largest mass configuration we find is $M_{TOV} = 1.99M_\odot$. Looking at the top left plot we can see that even though the two peaks present in Fig. 12 are obviously erased by demanding monotonicity, we still observe a rapid rise of the speed of sound in small energy densities. Furthermore the PDF indicates that the vast majority of solutions are of concave nature ($\frac{d^2}{de^2}\, c_s^2 < 0$) as they avoid the lower right of the parameter space completely. Given that no mass constraint is imposed we cannot account this increase to be a mere product of selection. Much rather, internal investigations have provided numerical evidence that this rapid rise is mostly caused by the theoretical boundary conditions discussed in Chapter 2. Looking at the EoS band in the top right, the most prominent feature is that the accepted solutions all arrive in the stiffer parts of the pQCD-EoS matching point. Due to the EoS being the integral of the squared sound speed we make the theoretical boundary conditions responsible for this observation too.

For the sake of completeness, we close the results chapter with our final biased computation using only EoSs whose c_s^2 is globally subconformal. Albeit we already portrayed the subset of subconformal solutions in the yellow contours of Fig. 12, as Fig. 15 shows these solutions are largely underrepresented in an agnostic computation (being only 0.03% of the whole sample) which motivated a dedicated computation solely for subconformal solutions. Interestingly, as can be seen in the top left of Fig. 17, similar to the agnostic computation of Fig. 12 the subconformal solutions also exhibit this funnel at around 500 MeV/fm$^{\mathbf{3}}$. In this case, we can account the rapid stiffening to the $2M_\odot$ constraint. It is interesting to see how this funnel is translated to the EoS space in the top right. As can also be seen in Fig. 2 of [54], like the monotonic solutions, the subconformal EoSs too only take on very stiff pressure values at the pQCD matching point. In the bottom right figure which displays Λ with respect to the mass, we can see that compared with the agnostic ensemble, the lower boundary of Λ is increased for the subconformal solutions.

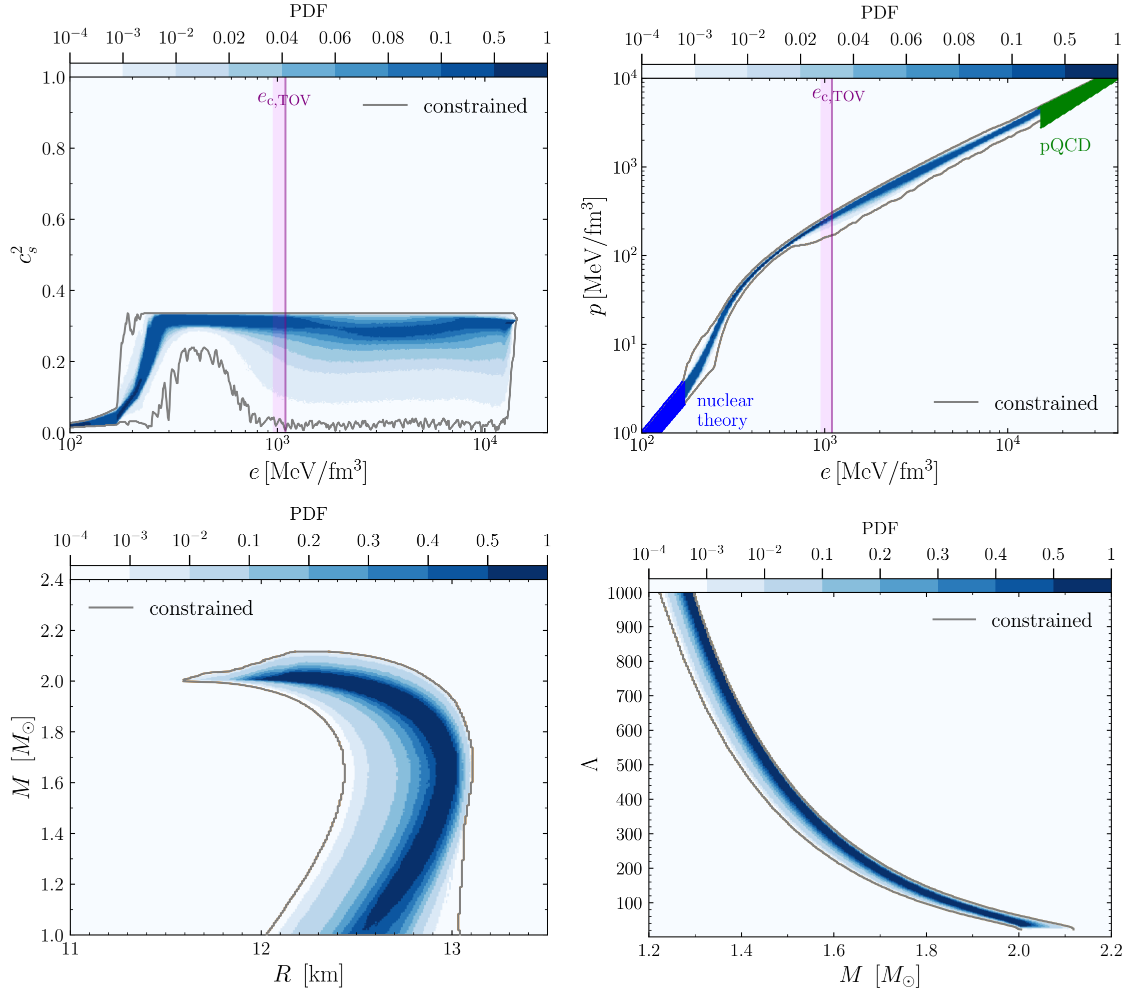

Figure 17: The same plot as in Fig. 12 but using only EoSs whose corresponding speed of sound is globally subconformal by construction. Both GW170817 and NICER constraints are imposed. Bottom left plot is baptized the ”stellar dolphin”.

5 Conclusion

The main goal of this thesis was to investigate the behaviour of the speed of sound in Neutron Stars. And to dive deeper: Are we able to exclude at least one of the three logical scenarios of the speed of sound explained in the introduction?

To answer this question, we have used the speed of sound interpolation method to generate $1.5 \cdot 10^7$ EoSs that are consistent with nuclear matter and pQCD calculations. Among those that are consistent with the data of GW170817 and the most recent NICER measurements, we analyzed the statistical distribution of the squared speed of sound, EoS, mass-radius and tidal deformability ensemble. We find that a steep rise of the speed of sound below e $\lesssim$ 500 MeV/fm$^{\mathbf{3}}$ turned out to be a robust observation independent of the prior, number of segments or filtering. Furthermore, our agnostic computation shows that the vast majority of solutions exhibit a robust peak $c_s^2 > 1/3$, thus showing a clear statistical preference towards superconformal solutions. In fact, only 0.03% of all constraint-satisfying solutions are subconformal. By conducting a separate computation containing only subconformal EoSs we were able to identify a lower bound $c_s^2 \gtrsim 0.2$ at $e \approx 500$ MeV/fm$^{\mathbf{3}}$. The largest mass supported by a subconformal solution lies at $M \approx 2.1 M_\odot$. Albeit still in agreement with the recent observational evidence, the discovery of a $M > 2.1 M_\odot$ Neutron Star would rule out the scenario of subconformal EoSs entirely. Through our statistical analysis, we were able to obtain estimates of Neutron Star radii for two representative masses of 1.4 and 2.0 solar masses, namely $R_{1.4} = 12.42^{+0.52}_{-0.99}$ km and $R_{2.0} = 12.11^{+1.11}_{-1.23}$ km and also for the binary tidal deformability of GW170817 $\tilde{\Lambda}_{1.186} = 483^{+224}_{-210}$ (All values at a 95% confidence level). Additionally, we provided an analytical estimate of the minimum and maximum binary tidal deformability with respect to the chirp mass. Interestingly, the distribution of our mass-radius relations are in remarkable agreement with analytical predictions on the minimum stellar radius. Refering back to the question asked in the paragraph above, we were indeed able to exclude one of the three scenarios discussed in the introduction, namely that EoSs corresponding to a globally monotonic speed of sound are not stiff enough to support $2M_\odot$ Neutron Stars and are thus most likely ruled out by the mass measurement of PSR J0740+6620. For future work, it would be necessary to implement improved pQCD constraints to the EoS recently proposed by [59]. Moreover, pursuing the same questions as this thesis but using alternate ways to parametrize the EoS like piecewise polytropes [39] or spectral parametrizations [60] could help determine a possible model-induced bias, which we expect to be small though. Lastly, extending this exercise to the case of uniformly or differentially rotating Neutron Stars would promise further interesting insights too.

A Impact of Segments on the Posterior

In this first part of the Appendix, we explore in more detail the methodological subtleties of the speed of sound interpolation method. In detail, we investigate the impact a different choice for the number of segments and sample size has on the posterior distributions as well as the impact of an artificial constraint proposed in [5].

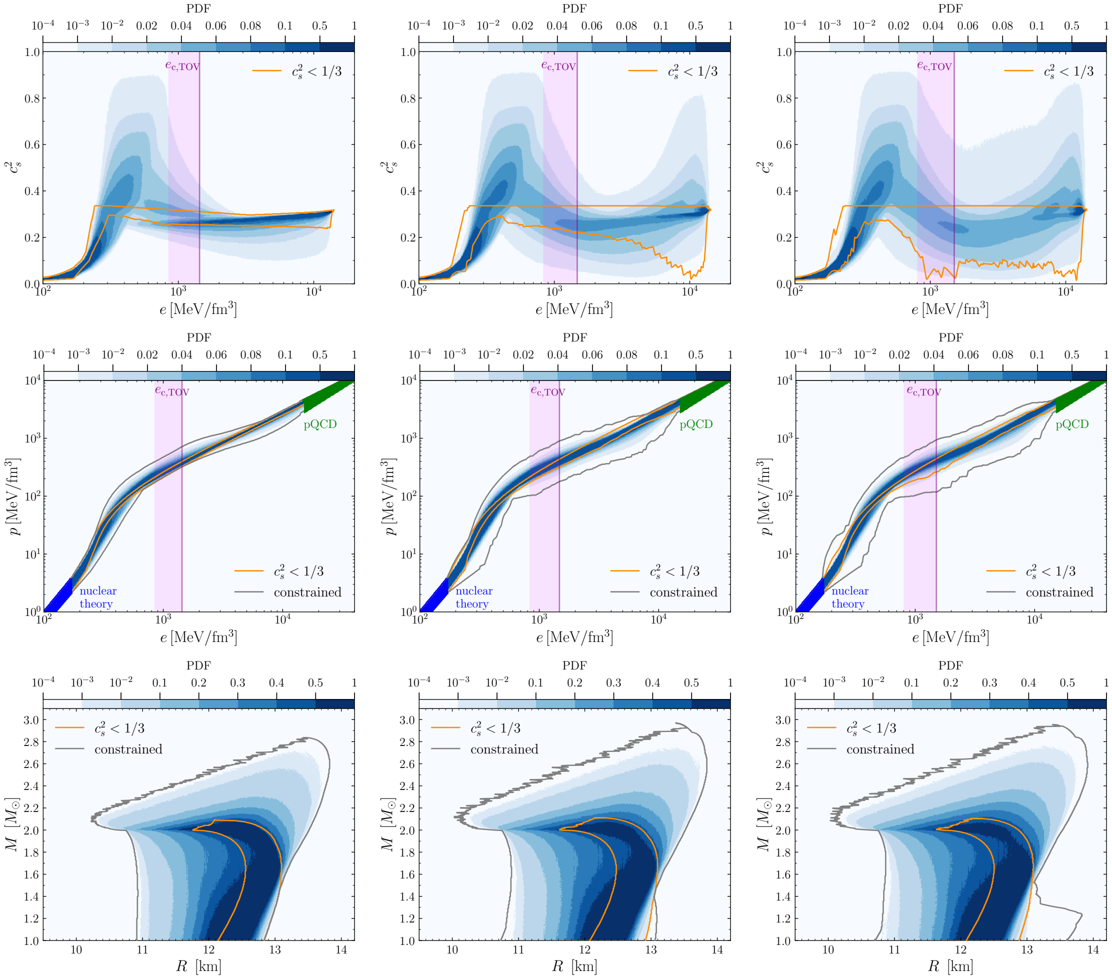

Figure 18: Top row: Squared speed of sound for 3,4,5 segments. Middle row: Corresponding EoSs. Bottom row: Corresponding MR relations. Yellow contours depict the envelope of the subconformal subset in all plots. NICER and GW170817 constraints are imposed.

The number of segments used is the main free parameter of the speed of sound interpolation method. This has motivated us to investigate how choosing a different number of segments impacts the posterior distributioons. In Fig. 18 we show the results of our computations when choosing 3-5 segments respectively. What immediately caught our attention in these plots is the behaviour of the speed of sound. While the first peak at low densities turns out to be a robust feature independent of the number of segments, the strange second peak is not present in the leftmost 3 segment computation. From this observation we conclude that the restricted geometrical possibilites three segments offer do not allow for a second peak when being consistent with the theoretical and observational constraints. While differences between the 4 and 5 segment computations can still be spotted, overall they are highly similar and foreshadow a convergent posterior distribution in the high-segment limit. We highlight this convergent behaviour in Fig. 19 where we show the outer envelope of all segment computations together. Although in the matter of the second peak the choice of three segments turned out to be beneficial, comparing the EoS ensemble the overall disadvantage of a low number of segments becomes evident. The gray envelope of the three segment computation is noteably thinner than those of the 4,5 segment computations. Furthermore, the deconfined phase transition is less pronounced in the former case. Thus we claim that three segments provide a too coarse description of the speed of sound and thus also for the EoS and MR space. Concluding our investigation of choosing different numbers of segments, we state that using a too low number of segments leads to a too restricted description of the EoS space. On the other hand, a larger number of segments gives rise to artifacts such as the unnatural second peak and are also more cost expensive from a numerical standpoint. Given the convergence we have portrayed in Fig. 19, using 7 segments as we did in all computations of Chapter 4 provided the best balance all advantages and disadvantages considered. A higher number of segments did not provide any noteable advantages.

Although the second peak is realized at energy densities larger than those present in Neutron Stars and is thus not expected to be realized in nature, it is still unnatural with respect to the behaviour of strongly interacting matter predicted by pQCD. Since we have shown in Fig. 18 that it can be seen as an artifact of the speed of sound interpolation method, one can be motivated to come up with a way to select out the models that cause it by means of being unnatural. In [5], an artificial constraint was introduced with the aim of sorting out solutions that exhibit a strongly fluctuating speed of sound in small energy density regimes. We implemented this constraint ourselves to see how it impacts the speed of sound distribution.

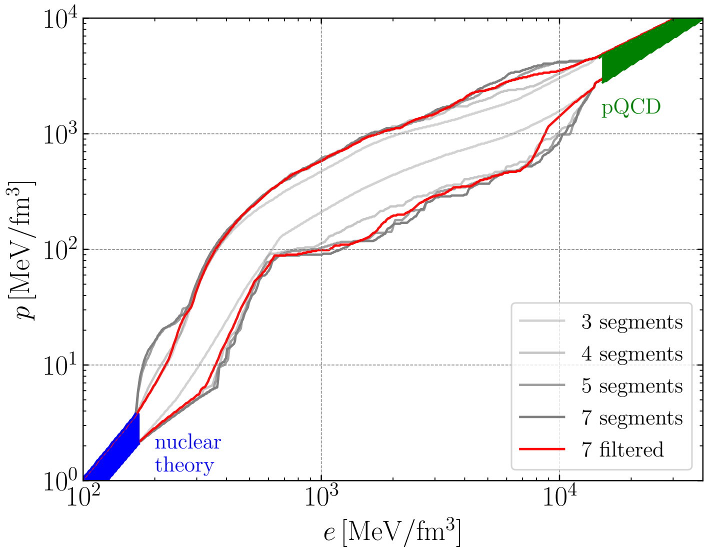

Figure 19: Shown is the convergence of the enclosing envelopes of five independent computations, varying the used number of segments as 3,4,5,7. The red envelope is the envelope coming from the computation that has the artificial constraint (57) implemented.

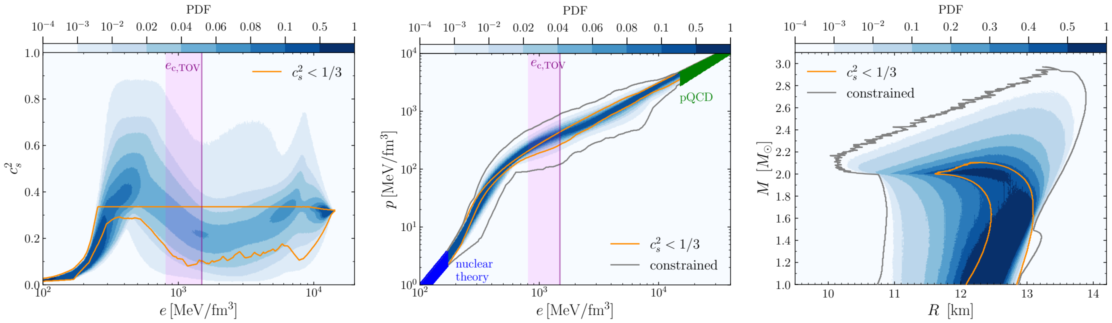

Figure 20: The result of our filtered computation using the artificial constraint (57). Seven segments are used and GW170817 and NICER constraints imposed.

In order to eliminate solutions with strongly fluctuating speed of sound, one can discard them if they satisfy the following condition for at least one pair of neighboured interpolants

$$e_{i+1} - e_i > \Delta ln(e) \cdot e_i \,, \tag{57}$$

where $\Delta ln(e)$ can be chosen as sufficient. In Fig. 20 we show our results when choosing $\Delta ln(e) = 0.5$. Although this condition seems to tame the second peak and eliminate strongly fluctuating behaviour at around e = 200 MeV/fm$^{\mathbf{3}}$ visible in Fig. 12 and Fig. 17, it has introduced additional artifacts in the high energy density regime. What we also find interesting, is that this condition suppresed the rightward hump in the MR plot, showing that this feature is caused by strongly fluctuating speed of sound profiles. This also explains why the hump is not very pronounced in the 4 segment computation, and non-existent in the 3 segment computation both visible in Fig. 18. A low number of segments is obviously not able to generate a strongly fluctuating sound speed.

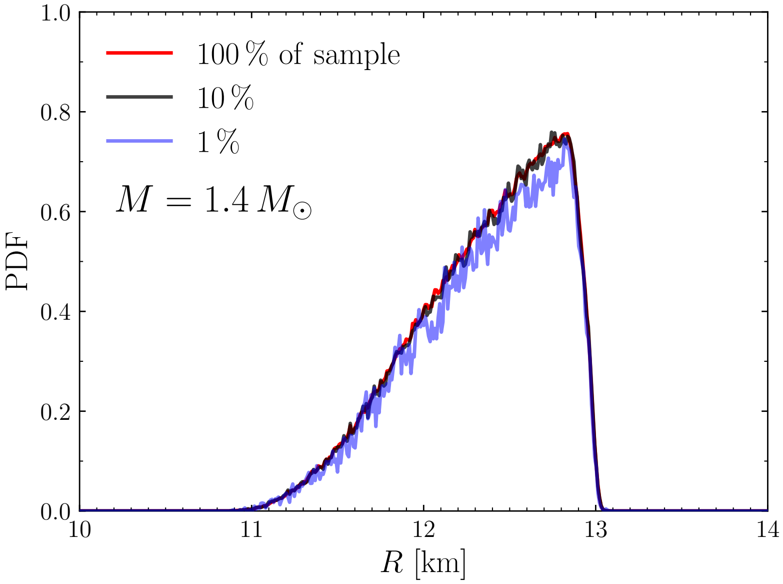

Figure 21: The radial PDF of the $M = 1.4M_\odot$ mass slice of our main 7 segment computation of Chapter 4. Shown are the PDFs when varying the sample size.

Given that we chose a statistical emphasis on the depiction of our data, we are motivated to analyze the convergence a subset of our whole sample size of $1.5 \cdot 10^7$ EoS yields. While the 1% PDF is already remarkably close to the full dataset, the

10% computation is already basically indistinguishable from the full dataset. Note though that the boundary of the data, marked as the gray contour in all our plots does depend more heavily on the sample size.

We close our discussion of Appendix A by considering the central energy density of all M_{TOV} configurations we have.

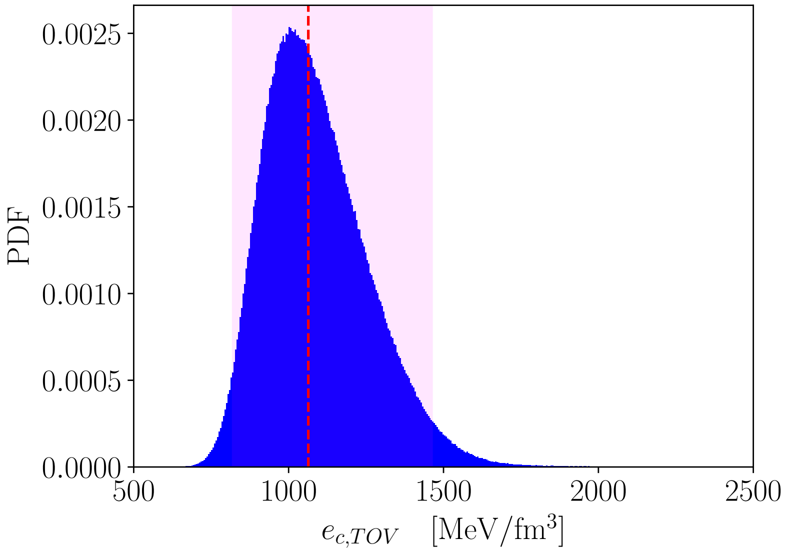

Figure 22: Shown is the distribution of all $e_{c,TOV}$ our constraint-satisfying ensemble (Fig. 12) offers. The red dashed line marks the median at e = 1063 MeV/fm^{3}. The purple envelope marks the 95% confidence interval 819-1462 MeV/fm^{3} identical to the one depicted in 12.

Fig. 22 reveals that the vast majority of central energy densities cluster around 819-1462 MeV/fm^{3} with a clear peak at $\approx$ 1030 MeV/fm^{3}. The boundary of the distribution lies between $e_{c,TOV,min} = 589$ MeV/fm^{3} and $e_{c,TOV,max} = 4451$ MeV/fm^{3} which is comparable to what is found in Fig. 6 of [5]. When isolating the EoSs that yield the $e_{c,TOV}$ of the reported boundary-values, we noticed that they exhibit a very strong phase transition. Due to this phase transition, trying to accurately resolve the M_{TOV} configuration by steadily increasing the initial central density is hard since the pressure does not change significantly. Because of that, one runs into the danger of running into the unstable branch of the MR curve and cannot accurately resolve the range of $e_{c,TOV}$. This is the reason why we compute the median of the distribution and use the 95% percentile ranges as the actual boundaries that we depict in all our plots as the vertical purple bands.

B Numerical Setup

B.1 RK4 Integrator

The numerical grunt work of this thesis lies in solving the TOV equations. As explained in Chapter 1.1 they only yield an analytical solution for the unrealistic case of constant energy density. Because of that, we have to solve the TOV equations numerically. Fortunately, we are dealing with a system of first order ordinary differential equations which can be integrated using a fourth order Runge-Kutta routine.

Since we are seeking the stellar solution P(r) for a given central density p_c, we start by discretizing the radial coordinate on an equidistant grid

$$r_i = r_{initial} + i \cdot \Delta r \quad i \in [0, N_{radial} - 1] \quad \Delta r = \frac{r_{end} - r_{initial}}{N_{radial} - 1} \,. \tag{58}$$

Because we do not know the radius of the star before the calculation has finished, a sufficiently high r_{end} is necessary. For $r_{initial}$, sufficiently low values have proven themselves to work. We are dealing with a system of four ODE's (11,12,50,51) that can be described as

$$\frac{d\vec{y}(r)}{dr} = \vec{f}(r, y) \quad \vec{y}(r) = (P(r), m(r), H(r), \beta(r))^T \quad \vec{y}(r_{initial}) = \vec{y_0} \,, \tag{59}$$

where $\vec{f}(r, y)$ makes up the right hand side of those ODE's. Starting from the known initial values at $\vec{y}(r_{initial})$ present in the center of the star, we can now integrate the pressure and mass outwards by using the recursive Runge-Kutta 4 relation

$$\vec{y}_{n+1} = \vec{y}_n + \frac{\Delta r}{6}\left(\vec{k}_1 + 2\vec{k}_2 + 2\vec{k}_3 + \vec{k}_4\right) \quad n \in [0, N_{radial} - 1] \,. \tag{60}$$

The vectors $\vec{k}_i$ are given by:

$$\vec{k}_1 = \vec{f}(r_n, y_n) \,, \tag{61}$$

$$\vec{k}_2 = \vec{f}(r_n + \frac{\Delta r}{2}, \Delta r \frac{\vec{k}_1}{2}) \,, \tag{62}$$

$$\vec{k}_3 = \vec{f}(r_n + \frac{\Delta r}{2}, \Delta r \frac{\vec{k}_2}{2}) \,, \tag{63}$$

$$\vec{k}_4 = \vec{f}(r_n + \Delta r, y_n + \Delta r \, \vec{k}_3) \,. \tag{64}$$

At some point in the outward integration, the radius will step out of the surface of the Neutron Star, resulting in a negative pressure. Thus, the condition $P(R) < 0$ will serve as a criterion to determine the radius of the Neutron Star. Its mass will then be given by $M_{NS} = m(R)$. The following plots display three different solutions to the TOV equations computed by the RK-4 algorithm outlined above:

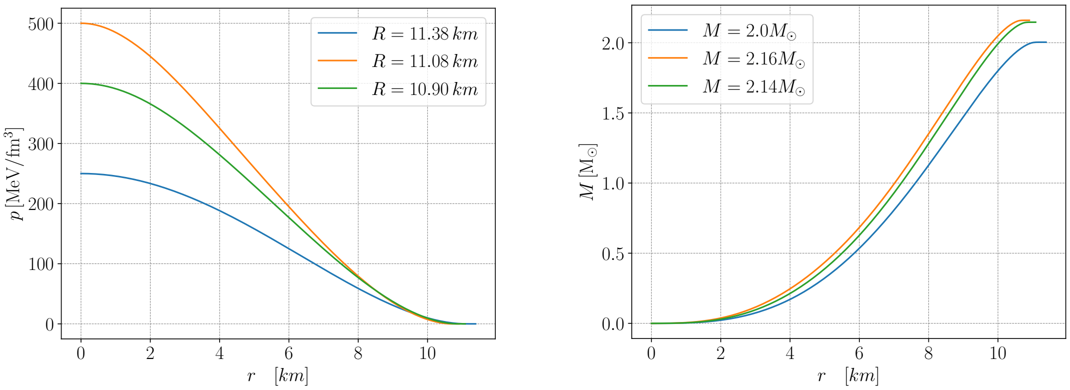

Figure 23: Three different solutions of the TOV equations obtained by using three different central pressures. Orange: 500 MeV/fm^3, Green: 400 MeV/fm^3, Blue: 250 MeV/fm^3

B.2 Numerical Implementation of the Pressure

While c_s^2 (31) and $n_B(\mu_B)$ (33) have closed analytical expressions and can thus be easily implemented numerically, the pressure (38) turned out to be relatively hard to implement analytically since numerical truncation errors led to non-vanishing imaginary parts of the hypergeometric function. Therefore we did not implement the analytical expression (38) in the code, but rather integrated $n_B(\mu_B)$ numerically (37) by using a simple trapezoidal rule where we discretize the chemical potential on an equidistant grid

$$h(\mu_B) = \frac{\mu_B - \mu_{CET}}{N-1}\,,\ \mu_0 = \mu_{CET}\,, \mu_N = 2.6\,GeV,\ \mu_\alpha = \mu_{CET} + \alpha \cdot \frac{\mu_N - \mu_{CET}}{N-1}\,, \tag{65}$$

$$p(\mu_B) = p_{CET} + \frac{h(\mu_B)}{2}[n_B(\mu_{CET}) + n_B(\mu_B)] + h(\mu_B)\sum_{\alpha=1}^{N} n_B(\mu_\alpha)\,. \tag{66}$$

B.3 The Rocky Path Towards a Viable Solution

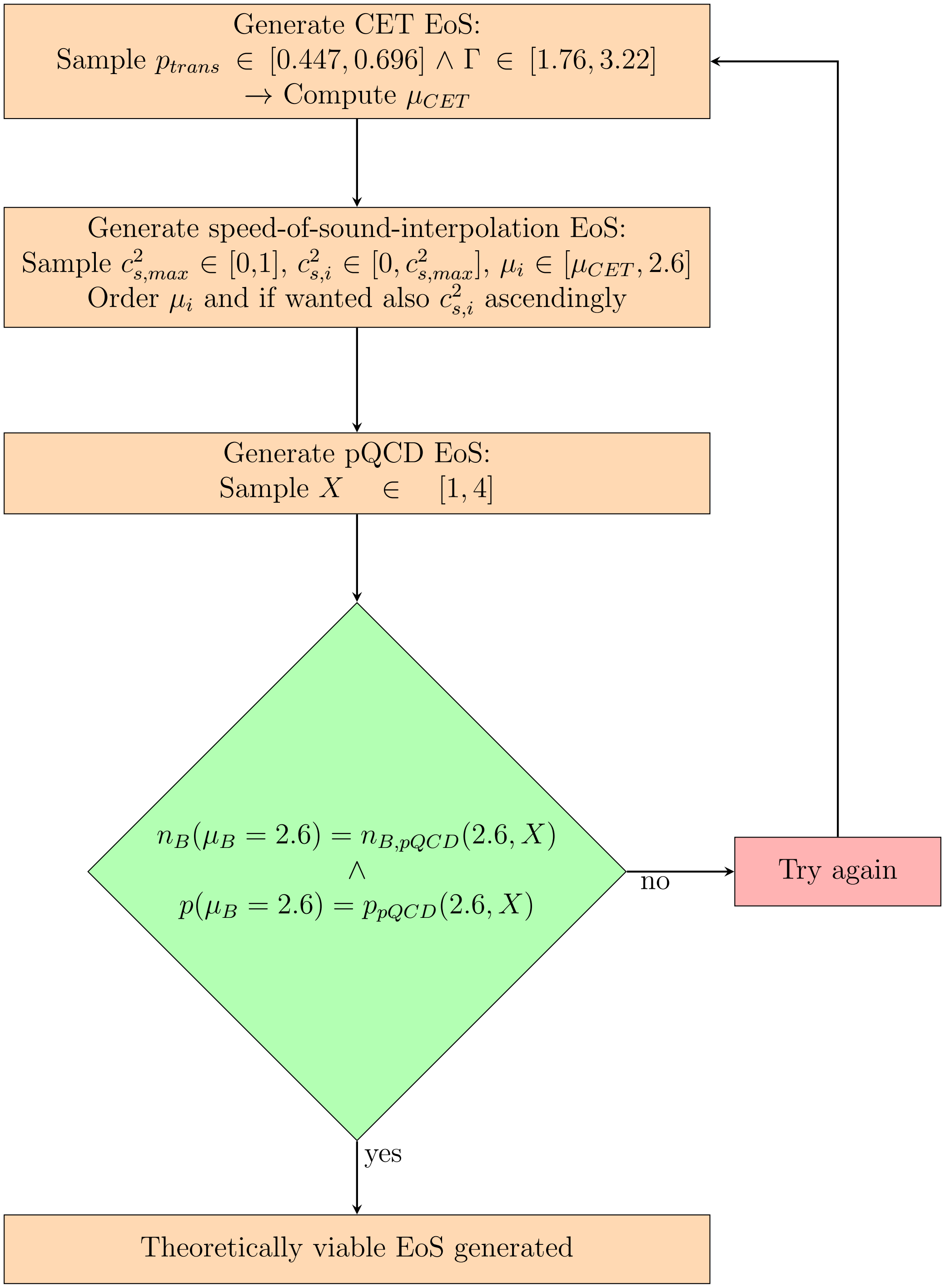

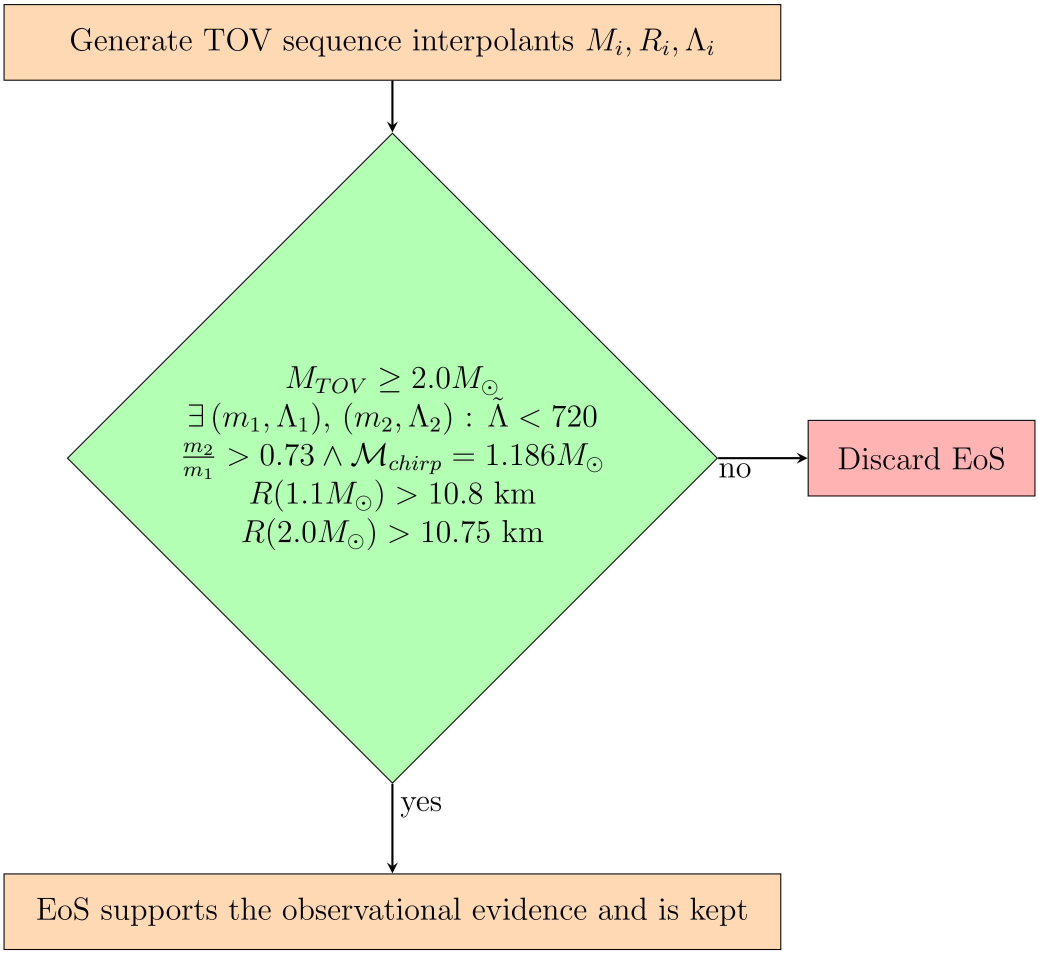

B.4 How we Compute the PDFs we are Using

As can be seen in our result plots, we have chosen a depiction of our data that emphasizes the statistical distribution of our set of solutions. To accomplish that, one has to come up with a two dimensional probability density function (PDF) that measures how many solutions are clustered within a given two-dimensional region with respect to the total number of solutions. Here, ”solution” refers to either an EoS, c_s^2, MR or Λ curve. In practice, finding a sensible way to define such a PDF turned out to be non-trivial. Also, there are certainly multiple different ways of accomplishing this. In what follows we briefly outline how we chose to construct the PDF for the example of the MR plot.

First of all, we set up an equidistant 2D grid $N_{mass} \cdot N_{radial}$, using $N_{radial} = N_{mass} = 700$ in this thesis through

$$M_i = M_{min} + i \cdot \frac{M_{max} - M_{min}}{N_{mass} - 1} \quad \wedge \; R_j = R_{min} + j \cdot \frac{R_{max} - R_{min}}{N_{radius} - 1} \,, \tag{67}$$

where the indices i and j denote each grid. The maximum and minimum values for each variable is chosen in a suitable way. The PDF is then of course a discrete function providing a numerical value for each bin

$$PDF(i,j) = \frac{bin(i,j)}{\Delta M \, \Delta R \, \sum_{i,j} bin(i,j)} \,. \tag{68}$$

ΔM and ΔR are defined by (67). bin(i,j) is a measure about how much weight is given to this specific bin. There are several ways one can compute the bin(i,j). The most simple way is to successively count how many distinct curves pass through the i-jth bin. This is the most straightforward way to relate the density of solutions passing through a space $\Delta M \cdot \Delta R$ with respect to the total number of solutions. One might criticise this approach as it gives equal weight to any curve that passes through each bin, not distinguishing between curves that only sparsely pass and ones that pass right through. Thus, one can modify bin(i,j) for example as the sum of the average values of every curve that passes through bin(i,j). As already said above, at this stage one can use several different approaches. At any rate, all of these approaches should yield the same PDF in the limit of small gridsizes, which we have observed for the two method explained in this paragraph, making them indistinguishable. We use approach (68) for all of our plots. When there are logarithmic axes involved, we simply change (67) such that it is linear on a logarithmic scale. It can be easily seen, that (68) is normalized since

$$\sum_{i,j} PDF(i,j) \cdot \Delta M \cdot \Delta R = \sum_{i,j} \frac{bin(i,j)}{\sum_{i,j} bin(i,j)} = 1 \,, \tag{69}$$

which is just the two-dimensional discretized integral of the whole space. Lastly, one can now easily extract mass and radii slices out of (68), turning it into a 1D PDF.

C List of Abbreviations

NS - Neutron Star

EoS - Equation of State

TOV - Tolman Oppenheimer Volkoff

CET - Chiral Effective Theory

pQCD - perturbative Quantum Chromodynamics

CFT - Conformal Field Theory

NICER - Neutron Star Interior Composition Explorer Mission

GW - Gravitational Wave

LIGO - Laser Interferometer Gravitational-Wave Observatory

PSR - Pulsating Source of Radiation

PDF - Probability Density Function

D Declaration of Authorship

I hereby declare that I have written the present thesis myself and without use of any other than the cited sources and aids. References with regard to the statement and scope are indicated by full details of the publications concerned. Some of the material presented in this thesis is part of a work with C. Ecker and L. Rezzolla [53]. This thesis was not yet, even in part, used in another examination or as a course performance.

Place, Date: ________________________ Signature: __________________

Eidesstattliche Erklärung

Hiermit versichere ich, dass ich die vorliegende Arbeit selbstständig und ausschließlich unter Benutzung der angegebenen Quellen und Hilfsmittel verfasst habe. Alle wörtlich übernommenen Sätze sind als Zitat und/oder Referenz belegt. Einige der in dieser Arbeit präsentierten Inhalte sind Teil einer Arbeit mit C. Ecker und L. Rezzolla [53]. Diese Arbeit wurde bisher weder in identischer noch ähnlicher Form einer Prüfungsbehörde vorgelegt und war bis jetzt nicht Gegenstand anderer Prüfungs- oder Studienleistungen.

Ort, Datum: ________________________ Unterschrift: __________________

References

[1] B. Abbott, R. Abbott, T. Abbott, F. Acernese, K. Ackley, C. Adams, T. Adams, P. Addesso, R. Adhikari, V. Adya and et al., *Properties of the binary neutron star merger gw170817*, *Physical Review X* **9** (Jan, 2019).

[2] S. Chandrasekhar, *On stars, their evolution and their stability*, *Rev. Mod. Phys.* **56** (Apr, 1984) 137–147.

[3] B. W. Carroll and D. A. Ostlie, *An Introduction to Modern Astrophysics*. 2nd (international) ed., 2007.

[4] J. R. Oppenheimer and G. M. Volkoff, *On massive neutron cores*, *Phys. Rev.* **55** (Feb, 1939) 374–381.

[5] E. Annala, T. Gorda, A. Kurkela, J. Nättilä and A. Vuorinen, *Evidence for quark-matter cores in massive neutron stars*, *Nature Phys.* **16** (2020), no. 9 907–910 [`1903.09121`].

[6] B. Kiziltan, A. Kottas, M. De Yoreo and S. E. Thorsett, *The neutron star mass distribution*, *The Astrophysical Journal* **778** (Nov, 2013) 66.

[7] J. Antoniadis, T. M. Tauris, F. Ozel, E. Barr, D. J. Champion and P. C. C. Freire, *The millisecond pulsar mass distribution: Evidence for bimodality and constraints on the maximum neutron star mass*, 2016.

[8] E. R. Most, L. R. Weih, L. Rezzolla and J. Schaffner-Bielich, *New constraints on radii and tidal deformabilities of neutron stars from gw170817*, *Physical Review Letters* **120** (Jun, 2018).

[9] C. D. Capano, I. Tews, S. M. Brown, B. Margalit, S. De, S. Kumar, D. A. Brown, B. Krishnan and S. Reddy, *Stringent constraints on neutron-star radii from multimessenger observations and nuclear theory*, *Nature Astronomy* **4** (Mar, 2020) 625–632.

[10] L. Rezzolla, P. Pizzochero, D. I. Jones, N. Rea and I. Vidaña, eds., *The Physics and Astrophysics of Neutron Stars*, vol. 457. Springer, 2018.

[11] J. M. Lattimer and M. Prakash, *The equation of state of hot, dense matter and neutron stars*, *Physics Reports* **621** (Mar, 2016) 127–164.

[12] K. Hebeler, J. M. Lattimer, C. J. Pethick and A. Schwenk, *Equation of state and neutron star properties constrained by nuclear physics and observation*, *The Astrophysical Journal* **773** (Jul, 2013) 11.

[13] A. Kurkela, E. S. Fraga, J. Schaffner-Bielich and A. Vuorinen, *Constraining neutron star matter with quantum chromodynamics*, *The Astrophysical Journal* **789** (Jun, 2014) 127.

[14] S. K. Greif, G. Raaijmakers, K. Hebeler, A. Schwenk and A. L. Watts, *Equation of state sensitivities when inferring neutron star and dense matter properties*, *Monthly Notices of the Royal Astronomical Society* **485** (mar, 2019) 5363–5376.

[15] I. Tews, J. Carlson, S. Gandolfi and S. Reddy, *Constraining the speed of sound inside neutron stars with chiral effective field theory interactions and observations*, *Astrophys. J.* **860** (2018), no. 2 149 [`1801.01923`].

[16] P. Bedaque and A. W. Steiner, *Sound velocity bound and neutron stars*, *Physical Review Letters* **114** (Jan, 2015).

[17] P. Bedaque and A. W. Steiner, *Sound velocity bound and neutron stars*, *Phys. Rev. Lett.* **114** (2015), no. 3 031103 [`1408.5116`].

[18] J. Alsing, H. O. Silva and E. Berti, *Evidence for a maximum mass cut-off in the neutron star mass distribution and constraints on the equation of state*, *Mon. Not. Roy. Astron. Soc.* **478** (2018), no. 1 1377–1391 [`1709.07889`].

[19] S. Carignano, L. Lepori, A. Mammarella, M. Mannarelli and G. Pagliaroli, *Scrutinizing the pion condensed phase*, *Eur. Phys. J. A* **53** (2017), no. 2 35 [`1610.06097`].

[20] S. Hands, S. Kim and J.-I. Skullerud, *Deconfinement in dense 2-color QCD*, *Eur. Phys. J. C* **48** (2006) 193 [`hep-lat/0604004`].

[21] L. McLerran and S. Reddy, *Quarkyonic matter and neutron stars*, *Physical Review Letters* **122** (mar, 2019).

[22] K. S. Jeong, L. McLerran and S. Sen, *Dynamically generated momentum space shell structure of quarkyonic matter via an excluded volume model*, *Physical Review C* **101** (mar, 2020).

[23] J. Margueron, H. Hansen, P. Proust and G. Chanfray, *Quarkyonic stars with isospin-flavor asymmetry*, *Phys. Rev. C* **104** (2021), no. 5 055803 [2103.10209].

[24] D. B. Blaschke, D. Gomez Dumm, A. G. Grunfeld, T. Klahn and N. N. Scoccola, *Hybrid stars within a covariant, nonlocal chiral quark model*, *Phys. Rev. C* **75** (2007) 065804 [nucl-th/0703088].

[25] T. Kojo, P. D. Powell, Y. Song and G. Baym, *Phenomenological QCD equation of state for massive neutron stars*, *Physical Review D* **91** (feb, 2015).

[26] C. Hoyos, N. Jokela, D. Rodríguez Fernández and A. Vuorinen, *Breaking the sound barrier in AdS/CFT*, *Phys. Rev. D* **94** (2016), no. 10 106008 [1609.03480].

[27] C. Ecker, C. Hoyos, N. Jokela, D. Rodríguez Fernández and A. Vuorinen, *Stiff phases in strongly coupled gauge theories with holographic duals*, *JHEP* **11** (2017) 031 [1707.00521].

[28] T. Demircik, C. Ecker and M. Järvinen, *Dense and Hot QCD at Strong Coupling*, 2112.12157.

[29] J. Antoniadis *et. al.*, *A Massive Pulsar in a Compact Relativistic Binary*, *Science* **340** (2013) 6131 [1304.6875].

[30] **NANOGrav** Collaboration, H. T. Cromartie *et. al.*, *Relativistic Shapiro delay measurements of an extremely massive millisecond pulsar*, *Nature Astron.* **4** (2019), no. 1 72–76 [1904.06759].

[31] E. Fonseca *et. al.*, *Refined Mass and Geometric Measurements of the High-mass PSR J0740+6620*, *Astrophys. J. Lett.* **915** (2021), no. 1 L12 [2104.00880].

[32] L. Rezzolla, E. R. Most and L. R. Weih, *Using gravitational-wave observations and quasi-universal relations to constrain the maximum mass of neutron stars*, *The Astrophysical Journal* **852** (jan, 2018) L25.

[33] A. Nathanail, E. R. Most and L. Rezzolla, *GW170817 and GW190814: Tension on the maximum mass*, *The Astrophysical Journal Letters* **908** (feb, 2021) L28.

[34] B. Margalit and B. D. Metzger, *Constraining the maximum mass of neutron stars from multi-messenger observations of GW170817*, *The Astrophysical Journal* **850** (nov, 2017) L19.

[35] M. T. Wolff *et. al.*, *NICER Detection of Thermal X-ray Pulsations from the Massive Millisecond Pulsars PSR J0740+6620 and PSR J1614-2230*, `2105.06978`.

[36] B. Abbott, R. Abbott, T. Abbott, F. Acernese, K. Ackley, C. Adams, T. Adams, P. Addesso, R. Adhikari, V. Adya and et al., *Gw170817: Observation of gravitational waves from a binary neutron star inspiral*, *Physical Review Letters* **119** (Oct, 2017).

[37] H. A. Buchdahl, *General relativistic fluid spheres*, *Phys. Rev.* **116** (Nov, 1959) 1027–1034.

[38] L. Rezzolla and O. Zanotti, *Relativistic Hydrodynamics.* 2013.

[39] J. S. Read, B. D. Lackey, B. J. Owen and J. L. Friedman, *Constraints on a phenomenologically parametrized neutron-star equation of state*, *Physical Review D* **79** (Jun, 2009).

[40] A. Bagdasaryan, *A note on the 2f1 hypergeometric function*, 2009.

[41] G. Baym, C. Pethick and P. Sutherland, *The Ground state of matter at high densities: Equation of state and stellar models*, *Astrophys. J.* **170** (1971) 299–317.

[42] E. S. Fraga, A. Kurkela and A. Vuorinen, *INTERACTING QUARK MATTER EQUATION OF STATE FOR COMPACT STARS*, *The Astrophysical Journal* **781** (jan, 2014) L25.

[43] A. Kurkela, P. Romatschke and A. Vuorinen, *Cold quark matter*, *Phys. Rev. D* **81** (May, 2010) 105021.

[44] V. Braun, G. Korchemsky and D. Müller, *The uses of conformal symmetry in QCD*, *Progress in Particle and Nuclear Physics* **51** (jan, 2003) 311–398.

[45] M. C. Miller *et. al.*, *The Radius of PSR J0740+6620 from NICER and XMM-Newton Data*, *Astrophys. J. Lett.* **918** (2021), no. 2 L28 [`2105.06979`].

[46] T. E. Riley *et. al.*, *A NICER View of the Massive Pulsar PSR J0740+6620 Informed by Radio Timing and XMM-Newton Spectroscopy*, *Astrophys. J. Lett.* **918** (2021), no. 2 L27 [2105.06980].

[47] T. E. Riley *et. al.*, *A NICER View of PSR J0030+0451: Millisecond Pulsar Parameter Estimation*, *Astrophys. J. Lett.* **887** (2019), no. 1 L21 [1912.05702].

[48] M. C. Miller *et. al.*, *PSR J0030+0451 Mass and Radius from NICER Data and Implications for the Properties of Neutron Star Matter*, *Astrophys. J. Lett.* **887** (2019), no. 1 L24 [1912.05705].

[49] T. Hinderer, B. D. Lackey, R. N. Lang and J. S. Read, *Tidal deformability of neutron stars with realistic equations of state and their gravitational wave signatures in binary inspiral*, *Physical Review D* **81** (Jun, 2010).

[50] T. Hinderer, *Tidal love numbers of neutron stars*, *The Astrophysical Journal* **677** (apr, 2008) 1216–1220.

[51] T. Damour and A. Nagar, *Relativistic tidal properties of neutron stars*, *Physical Review D* **80** (Oct, 2009).

[52] Flanagan and T. Hinderer, *Constraining neutron-star tidal love numbers with gravitational-wave detectors*, *Physical Review D* **77** (Jan, 2008).

[53] S. Altiparmak, C. Ecker and L. Rezzolla, *On the Sound Speed in Neutron Stars*, 2203.14974.

[54] E. Annala, T. Gorda, E. Katerini, A. Kurkela, J. Nättilä, V. Paschalidis and A. Vuorinen, *Multimessenger constraints for ultra-dense matter*, 2105.05132.

[55] S. Köppel, L. Bovard and L. Rezzolla, *A general-relativistic determination of the threshold mass to prompt collapse in binary neutron star mergers*, *The Astrophysical Journal* **872** (feb, 2019) L16.

[56] J. C. Jiménez and E. S. Fraga, *Radial oscillations in neutron stars from QCD*, *Phys. Rev. D* **104** (2021), no. 1 014002 [2104.13480].

[57] E. R. Most, A. Nathanail and L. Rezzolla, *Electromagnetic emission from blitzars and its impact on non-repeating fast radio bursts*, *The Astrophysical Journal* **864** (sep, 2018) 117.

[58] S. Huth *et. al.*, *Constraining Neutron-Star Matter with Microscopic and Macroscopic Collisions*, 2107.06229.

[59] O. Komoltsev and A. Kurkela, *How perturbative QCD constrains the Equation of State at Neutron-Star densities*, 2111.05350.

[60] L. Lindblom and N. M. Indik, *Spectral approach to the relativistic inverse stellar structure problem*, *Physical Review D* **86** (oct, 2012).